instruments

MDPI

Article

Commissioning of a High Pressure Time Projection Chamber with Optical Readout

Alexander Deisting [1,*], Abigail Victoria Waldron [2,*], Edward Atkin [2], Gary Barker [3], Anastasia Basharina-Freshville [4], Christopher Betancourt [5], Steven Boyd [3], Dominic Brailsford [6], Zachary Chen-Wishart [1], Linda Cremonesi [4,†], Adriana Dias [1], Patrick Dunne [2], Jennifer Haigh [3], Philip Hamacher-Baumann [7], Sebastian Jones [4], Asher Kaboth [1], Alexander Korzenev [8], William Ma [7], Philippe Mermod [8,‡], Maria Mironova [2,9], Jocelyn Monroe [1], Ryan Nichol [4], Toby Nonnenmacher [2], Jaroslaw Nowak [6], William Parker [1,§], Harrison Ritchie-Yates [1], Stefan Roth [7], Ruben Saakyan [4], Nicola Serra [5], Yuri Shitov [2,10], Jochen Steinmann [7], Adam Tarrant [1,||], Melissa Uchida [2,11], Sammy Valder [3], Mark Ward [7,12] and Morgan O. Wascko [2]

1   Department of Physics, Royal Holloway, University of London, Egham Hill, Egham TW20 0EX, UK; Zachary.Chen-Wishart.2016@live.rhul.ac.uk (Z.C.-W.); Adriana.Dias.2011@live.rhul.ac.uk (A.D.); Asher.Kaboth@rhul.ac.uk (A.K.); jocelyn.monroe@rhul.ac.uk (J.M.); william.parker@physics.ox.ac.uk (W.P.); Harrison.Ritchie-Yates.2013@live.rhul.ac.uk (H.R.-Y.); A.Tarrant@liverpool.ac.uk (A.T.)
2   The Blackett Laboratory, Imperial College London, London SW7 2BW, UK; e.atkin17@imperial.ac.uk (E.A.); p.dunne12@imperial.ac.uk (P.D.); maria.mironova@physics.ox.ac.uk (M.M.); toby.nonnenmacher14@imperial.ac.uk (T.N.); Shitov@JINR.ru (Y.S.); m.a.uchida@imperial.ac.uk (M.U.); m.wascko@imperial.ac.uk (M.O.W.)
3   Department of Physics, University of Warwick, Coventry CV4 7AL, UK; g.j.barker@warwick.ac.uk (G.B.); S.B.Boyd@warwick.ac.uk (S.B.); J.Haigh.2@warwick.ac.uk (J.H.); s.valder@warwick.ac.uk (S.V.)
4   Department of Physics, University College London, Gower St, Kings Cross, London WC1E 6BT, UK; anastasia.freshville@ucl.ac.uk (A.B.-F.); l.cremonesi@qmul.ac.uk (L.C.); sebastian.jones.17@ucl.ac.uk (S.J.); r.nichol@ucl.ac.uk (R.N.); r.saakyan@ucl.ac.uk (R.S.)
5   Physik-Institut, Universität Züriche, Rämistrasse 71, 8006 Zürich, Switzerland; christopher.betancourt@cern.ch (C.B.); nicola.serra@cern.ch (N.S.)
6   Department of Physics, Lancaster University, Bailrigg, Lancaster LA1 4YW, UK; d.brailsford@lancaster.ac.uk (D.B.); j.nowak@lancaster.ac.uk (J.N.)
7   III. Physikalisches Institut, RWTH Aachen University, 52056 Aachen, Germany; hamacher.baumann@physik.rwth-aachen.de (P.H.-B.); ma@physik.rwth-aachen.de (W.M.); stefan.roth@physik.rwth-aachen.de (S.R.); jochen.steinmann@physik.rwth-aachen.de (J.S.); mark.ward@snolab.ca (M.W.)
8   Department of Physics, DPNC Université de Genève, 1205 Genf, Switzerland; korzenev@mail.cern.ch
9   Department of Physics, Oxford University, Oxford OX1 3PU, UK
10   JINR, 141980 Dubna, Russia
11   Cavendish Laboratory, Cambridge CB3 0HE, UK
12   Department of Physics, Queen's University, Kingston, ON K7L 3N6, Canada
*   Correspondence: alexander.deisting@cern.ch (A.D); a.waldron@imperial.ac.uk (A.V.W.)
†   Current address: Department of Physics, Queen Mary University of London, Mile End Road, London E1 4NS, UK.
‡   Prof. Philippe Mermod passed away on 20 August 2020 during the course of the preparation of the paper. Dr. Alexander Deisting confirmed that he fulfilled the authorship criteria and he had no conflict of interest for the paper.
§   Current address: Clarendon Laboratory, Department of Physics, University of Oxford, Parks Road, Oxford OX1 3PU, UK.
|| Current address: The Oliver Lodge Laboratory, Department of Physics, University of Liverpool, Liverpool L69 7ZE, UK.

Abstract: The measurements of proton–nucleus scattering and high resolution neutrino–nucleus interaction imaging are key in reducing neutrino oscillation systematic uncertainties in future experiments. A High Pressure Time Projection Chamber (HPTPC) prototype has been constructed and operated at the Royal Holloway University of London and CERN as a first step in the development of a HPTPC that is capable of performing these measurements as part of a future long-baseline neutrino oscillation experiment, such as the Deep Underground Neutrino Experiment. In this paper, we describe the design

and operation of the prototype HPTPC with an argon based gas mixture. We report on the successful hybrid charge and optical readout using four CCD cameras of signals from [241]Am sources.

1. Introduction

High Pressure Time Projection Chambers (HPTPCs) are an area of growing international interest. The Deep Underground Neutrino Experiment (DUNE) envisions the use of an HPTPC as part of its near detector, and European groups have held a series of workshops on HPTPC development over the past five years. Given the recent indication of non-zero CP violation in the Tokai to Kamioka (T2K) experimental data [1], it is timely to quantify the potential impact of HPTPC neutrino (ν) detector technology on the mitigation of the dominant neutrino–interaction cross-section uncertainties for the future long-baseline neutrino oscillation programme.

Final State Interactions (FSIs) of nucleons that are produced in neutrino interactions are among the leading sources of systematic uncertainties in neutrino oscillation experiments [2]. Gas TPCs are ideal for precisely characterizing FSI effects because of their high track reconstruction efficiency, low momentum threshold, and 4π angular coverage of final state particles, which are all key in distinguishing between the different interaction models. For example, the proton multiplicity and momentum distributions for neutrino charged current interactions on argon that are calculated by the neutrino interaction Monte Carlo generators NEUT [3] and GENIE [4] are highly discrepant in the fraction of events with few ejected protons, and at low proton momentum, below 250 MeV/c [5]. This is below the proton detection threshold in water Cherenkov detectors (1100 MeV/c), and it is below that of liquid argon TPCs, approximately 400 MeV/c [6]. However, a gas-filled HPTPC has a low enough momentum threshold to resolve FSI model discrepancies and, therefore, an HPTPC has the unique capability to address the dominant systematic uncertainty in neutrino oscillation measurements.

This paper describes the design, commissioning, and calibration of a prototype HPTPC detector. Section 1.1 describes the prototype detector and readout design, Section 2 motivates the choice of gas target, Section 3 describes the high pressure vessel and the gas system, Section 4 details the TPC hardware, including its high voltage supply and data acquisition system. In Sections 5 and 6, the analysis of camera images and charge signal waveforms, respectively, are explained, and the results of the commissioning measurements are presented. Section 7 contains a combined analysis of the optical and charge readout signals.

1.1. Design Considerations

The need for lower momentum measurements [5] has motivated the choice of a gas-filled detector for the task of measuring neutrino-nucleus scattering. Another key consideration for the detector is that it has sufficient target mass to achieve a low statistical error on the measured final state kinematic distributions. This requirement drives the choice of a high pressure gas, as it has higher density and, therefore, higher mass.

The momentum threshold goal for our HPTPC prototype is designed to probe the discrepant low-momentum region of parameter space [5]. The threshold goal for a well-reconstructed proton in argon at 5 barA (10 barA) is ~50 MeV/c (approximately 70 MeV/c). This drives choices in the readout design, such that a proton track is sampled by ~10 measurements in the readout plane at ~50 MeV/c. We also aim to cover the momentum range above 320 MeV/c (50 MeV kinetic energy), where no measurements currently exist [5].

The track length of a 50 MeV/c proton in a 5 barA argon target is ~10 mm. A readout plane with a granularity of order 1 mm^2 is needed in order to achieve 10 samples along such a track. Conventional segmented pad planes of current experiments (e.g., T2K) have a

pad size of around $1\,\text{cm}^2$ at the cost of approximately 8 EUR per channel. A solution with a lower cost per channel is attractive given that an area of $20\,\text{m}^2$ is realistic for the readout plane of a future HPTPC near detector in a long-baseline neutrino oscillation experiment.

The transverse diffusion in pure Ar at 5 barA is too large to allow drift lengths of several 10 cm while permitting 1 mm track sampling. When adding a quencher, such as CO_2, to the argon gas, the diffusion is reduced, allowing for 1 mm track sampling and a 50 cm drift length (Section 2).

1.2. Optical Readout

Optical readout is a relatively new development in TPC readout technology that offers a low cost per channel. TPCs have been in use since the late 1970s, typically with the direct readout of the drifted charge. CCD optical readout of time projection chambers was first demonstrated in ~1990 by [7–9], and it has more recently been developed by the DMTPC project for direction-sensitive dark matter searches [10], by the CYGNO collaboration [11], by an optical TPC for precision nuclear physics cross section measurements [12], for X-ray imaging [13], for proton imaging [14], and by the CERN gas detectors group for radiography using X-rays [15]. DMTPC demonstrated that a TPC with optical readout can realize a sub-mm^2 segmentation over a readout plane with an area larger than $1\,\text{m}^2$ [16]. We refer the reader to [17] for a recent review.

An optical TPC is instrumented with a cathode and (several) anode electrodes that define its signal collection and amplification regions. Figure 1 shows a schematic of how our optical TPC operates. Ionisation electrons from charged particles propagating through the TPC move in the drift field to the amplification region, where avalanche charge multiplication and scintillation photon production occur (Figure 1a). The anodes may also be equipped with charge readout to provide high resolution tracking in the drift direction, as in [16]. CCD or CMOS cameras view the amplification plane through lenses from outside of the (pressure) vessel containing the TPC and target gas, collecting the scintillation light, and subsequently providing tracking information in the amplification plane. The design considerations for optical TPCs are described in detail in [17].
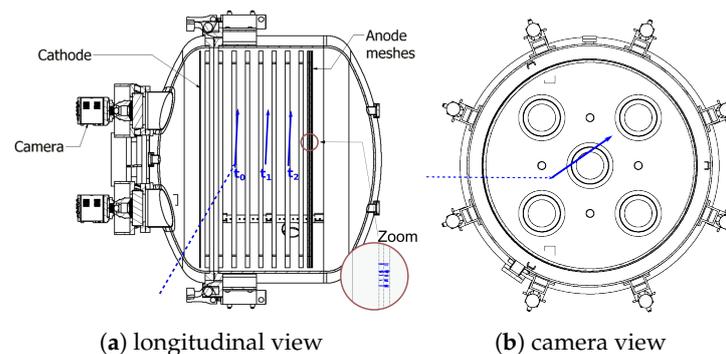

(**a**) longitudinal view   (**b**) camera view

Figure 1. Cross-sectional view of the HPTPC through (**a**) the plane parallel to the drift field *E* and (**b**) the plane perpendicular to *E*. A particle (dotted line) scatters on an atom or molecule in the gas at the time t_0, ejects a charged particle from the nucleus, which, in turn, ionizes gas atoms along its trajectory (arrow, Figure (**a**)). These ionization electrons are moved by *E* towards the anode meshes and they are eventually amplified. The positions of these ionization electrons as they drift are labelled t_1 and t_2. Photons that are produced during the amplification are then imaged by cameras and provide the 2D projection of the interaction (Figure (**b**)), the zoomed inlet in (**a**) illustrates where avalanches form and the photons are emitted.

In an optical TPC, the track reconstruction resolution in the amplification plane depends on the optical plate scale. The requirement that the object be in focus determines this scale, which sets the minimum object distance in consideration of the image distance and focal length of the lens, as well as the optical system demagnification, which is the

ratio of the object to image distances. Typical demagnification values are 5–10. The area of the amplification region that is imaged by each CCD pixel determines the smallest unit of track segment measurement possible with a given optical system and detector geometry. We define a *vixel* to be a box with an area of A_{vixel} in the readout plane and a height corresponding to the length that an electron drifts during one CCD exposure time.

The transverse diffusion of the ionization electrons from a particle track in the TPC determines the minimum sensible vixel size, as they drift to the amplification region. The number of samples along the track determines the track reconstruction resolution in the drift direction, which depends on the track length, drift velocity, and readout rate.

The momentum threshold for track reconstruction depends on the minimum deposited energy at which a cluster of vixels can be identified as a track. This primarily depends on the signal-to-noise ($\mathcal{S} : \mathcal{N}$) ratio per vixel. In general, vixels with $\mathcal{S} : \mathcal{N} > 5$ can be identified as part of a particle track [18].

The expected signal size, which is the number of photons collected per pixel, is given by

$$
N_{\mathcal{S}} = \left[\frac{\varepsilon_{\text{particle}}}{W} \times G \times (\gamma/e^-) \right] \times \left[T_{\text{anode}} \times T_{\text{cathode}} \times T_{\text{window}} \times T_{\text{lens}} \right]
$$
$$
\times \left[\frac{1}{16 \times f_{\text{stop}}^2 \times (1 + m_{\text{d}})^2} \right] \times QE^* \quad,
\tag{1}
$$

where the first term in brackets is the number of photons produced in the amplification region, which depends on the ionization energy that is deposited per vixel by a particle with energy $\varepsilon_{\text{particle}}$, the energy to liberate one electron-ion pair in the gas W, the gas amplification factor (gain) G, and the scintillation photon-to-electron ratio (γ/e^-) of the gas. The total photon transmission of the system is the second term in brackets, which depends on the transmittance of the lens (T_{lens}), the pressure vessel window (T_{window}), and the cathode (T_{cathode}) and anode meshes (T_{anode}) through which the CCD views the amplification region, which is averaged over the scintillation emission spectrum. The geometric acceptance of the optical system is the third term in brackets, which depends on the lens aperture to focal length ratio (f_{stop}) and the demagnification (m_{d}). The last term QE^* is the CCD quantum efficiency that is averaged over the scintillation emission spectrum. Other elements that enhance (e.g., reflections) or reduce the signal are not taken into account.

The noise per vixel depends on the quadrature sum of the shot noise, which is $\sqrt{N_{\text{signal}}}$, the read noise N_{read}, and the dark rate of the camera times the exposure time ($N_{\text{pixels}} \cdot R(T) \cdot t_{\text{exposure}}$):

$$
N_{\mathcal{N}} = \sqrt{N_{\text{signal}} + N_{\text{read}}^2 + N_{\text{pixels}} \cdot R(T) \cdot t_{\text{exposure}}} \quad.
\tag{2}
$$

In the dark noise term, N_{pixels} is the number of CCD pixels grouped into a readout bin, t_{exposure} is the exposure time of a pixel, and $R(T)$ is the dark rate, which is a function of temperature T. Here, a readout bin is a collection of camera pixels grouped together and read out as one. Typically, a cooled CCD can suppress the dark current to < 0.1 electrons/pixel/s, whilst the read noise is around 10 electron RMS, so, for exposure times of an order of seconds, the read noise dominates. The area determined by $N_{\text{pixels}} \times A_{\text{vixel}}$ can be thought of as an effective pad size of the readout, where A_{vixel} is the vixel area that is imaged by one CCD pixel.

In the prototype detector that is described here, the vixel size is $\sim 236 \times 236\,\mu\text{m}^2$ in the readout plane, and the readout binning operated was 4×4 ($N_{\text{pixels}} = 16$) and 8×8 ($N_{\text{pixels}} = 64$), which produced an effective pad size after readout binning of $\sim 0.86\,\text{mm}^2$ and $\sim 3.46\,\text{mm}^2$, respectively. In this way, a 10 mm long track, which corresponds to a 50 MeV/c proton, is sampled at 5–10 points, because the vixel area in the readout plane is a square. The area A_{vixel} is calculated by dividing the area that is imaged by one camera

($\sim$71 $\times$ 71 cm^2) by the camera's pixel layout of 3056 $\times$ 3056 pixel^2 and accounting for the readout binning. The height of a vixel corresponds to the full drift length, because we operated the cameras with an exposure time of 0.5 s to 1 s.

1.3. HPTPC Prototype Overview

The prototype HPTPC detector that is described here is housed in a stainless steel (type 304L) vessel (Section 3) of volume 1472 L, which is rated to 5 barG. We use barA to denote the absolute pressure and barG for pressure measurements relative to ambient pressure. The vessel features feed-through for high voltage and instrumentation, optical windows, and camera mounting hardware. Figure 1 sketches the detector layout. The vessel's internal rail system supports a TPC, which has 44.7 cm drift length and 111 cm diameter (Section 4). The TPC drift region is enclosed by the cathode mesh at a negative voltage and the first anode mesh. Two more anode meshes at increasing positive voltage follow in order to amplify primary ionizations.

Figure 1 illustrates the working principle of the detector. A particle entering the drift volume (e.g., a neutrino) scatters at a time t_0 on an atom or molecule, thereby ejecting protons from the struck nucleus. These final state particles ionize gas atoms and molecules along their path (indicated schematically with an arrow in Figure 1a). The resulting primary ionization electrons drift in the electric field E towards the anode meshes and are eventually amplified in the high electric field close to the meshes' wires and between the meshes. In the avalanche, electrons and photons are produced and the cameras can then record the latter, which provide an image of the interaction (Figure 1b) with the locations as well as the intensity, where the latter is proportional to the energy that is deposited in the drift volume. Reading out the charge signals that are induced by the avalanches at the anode meshes provides additional time information. The duration of these charge signals in the anodes will be proportional to the track length that is projected into the drift direction. The advantages of using this charge readout include the ability to calibrate gas mixtures that emit very little light and the ability to correlate light and charge signals.

The optical readout system for the HPTPC prototype that is described here uses four CCD cameras, which are mounted onto the high pressure vessel and image the amplification stage from the cathode side, through the windows of the pressure vessel, as well as through the cathode and anode meshes. Each camera views one quadrant of the amplification region, through lenses that are focused on the amplification plane (Section 4.6). The HPTPC's charge readout system reads the charge that is induced on the whole (un-segmented) plane of each of the three anodes. Commercial front end electronics decouple, amplify, and shape the signals, and they are subsequently digitized synchronously in time with the CCD data acquisition. Throughout the paper, we use a Cartesian coordinate system in which all of the electrodes are x/y planes at a constant z and where the z axis is parallel to the electric field direction. The origin is located in the center of the anode 1 mesh and z increases towards the cathode. In the x/y planes, we occasionally use polar coordinates, where r points from the center to the edge of the TPC.

2. Gas Requirements

The typical wavelength sensitivity range of CCD cameras is 350 nm to 850 nm (Section 4.6) and, therefore, the gas is required to have a high photon (or electro-luminescence) yield in this wavelength range. A noble gas is the obvious choice for the dominant part of the gas mixture, since it lacks the rotational and vibrational degrees of freedom that absorb photons.

Gaseous argon has been shown to emit not only light in the Vacuum Ultra Violet (VUV), but also in the near infra-red (NIR) wavelengths [19]. Scintillation light measurements at pressures that are higher than 1 barA show that the NIR light yield normalized to the number of amplification electrons decreases with increasing pressure [20]. However, this can be compensated by a larger gain of the amplification stage. In [20], the authors show that additions of CF_4 lead to a high photon yield in the visible (VIS) and NIR: in Ar gas

with a small (5%) admixture of CF_4, the scintillation photon yield in optical wavelengths is 0.1–0.3 per avalanche electron, and it is a weak function of the reduced electric field. Neon, on the other hand, also emits in the NIR region [21]. Admixtures of nitrogen have been shown to result in a higher intensity electro-luminescence in the VIS, as compared to the NIR neon electro-luminescence. Therfore, a Ne/N_2 mixture is also a good candidate for a TPC with optical readout.

We chose argon as the principle component of our gas mixture, because an Ar based mixture is foreseen for the HPTPC of DUNE's near detector. Demonstrating the technological readiness of an HPTPC with this gas mixture makes a strong case for the use of this technology as part of a near detector in a long-baseline neutrino oscillation experiment with far detectors with identical targets. Argon has already been proven to emit light at a high pressure in the wavelength range to which our cameras are sensitive [22]. Furthermore, argon is considerably less expensive than neon gas.

Operating a TPC with pure argon comes with the disadvantage that stable operation is notoriously difficult at high gains and the transverse diffusion is high. For a drift field of ∼200 V cm^{-1}, the transverse diffusion in pure Ar at 5 barA ($E/P \sim 0.05$ V/cm/Torr) is approximately 1000 µm/$\sqrt{cm}$ [23], as can be seen in Figure 2. An optical readout with cameras provides an effective segmentation of the readout plane into segments of less than a 1 mm^2, as discussed in Section 1.1. The diffusion in pure argon for drift lengths of several 10 s of cm is too large to exploit the advantages of a fine segmentation. Adding a quencher reduces the diffusion and enables higher gains under more stable operating conditions. For example, in Ar/CO_2 (99/1), the diffusion is reduced by an order of magnitude when compared to pure argon (Figure 2). This allows for drift lengths of up to 50 cm whilst retaining the requirement that the transverse diffusion does not exceed twice the readout segment length of 1 mm.
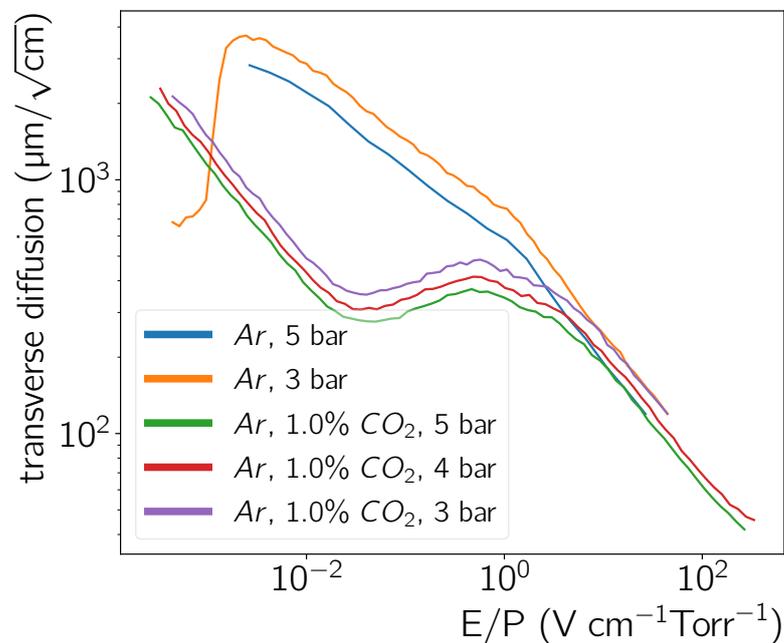

Figure 2. Transverse diffusion for pure argon and different Ar/CO_2 mixtures that were simulated using MAGBOLTZ [23].

Carbon-dioxide is the typical quencher for an Ar mixture; however, CO_2 has been shown to lower the light yield [22]. On the other hand, N_2 is not a good quencher in Ar, but it provides a small reduction in the light yield [22]. In this paper, we experimented with pure Ar and different Ar/CO_2, Ar/N_2, and $Ar/CO_2/N_2$ mixtures to establish which

gas provides the largest light gain in the NIR (Section 5.4). During the operation of the high pressure TPC, periods of sparking occurred (Section 5.1), which had a large influence on the choice of gas that was eventually used in the measurements presented in this paper. Other gases and admixtures are also interesting topics of study; however, these studies are not part of the measurements for this paper.

3. High Pressure Vessel Design

Figure 3 shows the pressure vessel design. The vessel is 304L stainless steel, with an inner (outer) diameter of 140 cm (142 cm). The total length of the vessel, including the domed ends, is 138.6 cm; the length of each domed section is 32.5 cm, leaving a length of 73.6 cm in the cylindrical straight section that hosts the TPC. The weight of the empty vessel is 2370 kg.
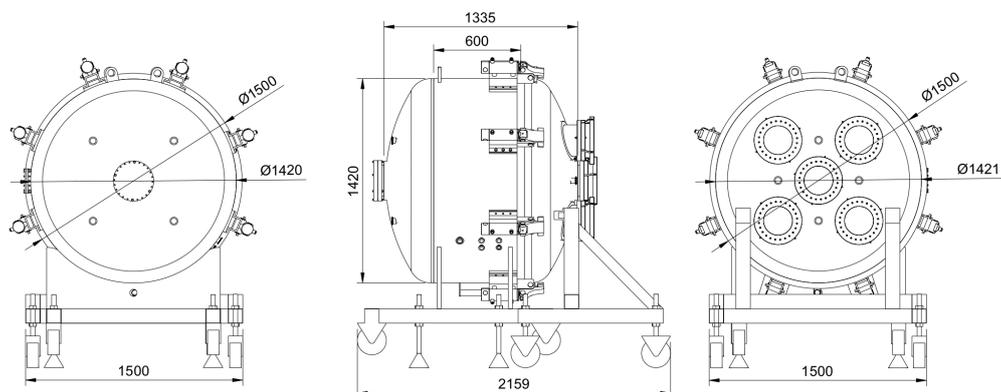

Figure 3. Schematic drawings of the pressure vessel: end view of the back side (**left**), side view with the vessel door to the right (**middle**), and end view of the door side (**right**).

One of the domed ends of the cylinder is fully detachable in order to gain access to the vessel's interior, e.g., for the TPC installation. The detachable door is connected to the body of the vessel via a large DN 1500 flange. The door and the body of the vessel are mounted to separate steel frames with wheels, both with adjustable feet for elevation adjustment. A double O-ring seal of viton and a rectangular silicone layer between the door and body flange sides provide gas tightness. The door and body flanges are clamped together with eight hydraulic pistons and eight screwable clamps, with a force up to 50 N m. The helium leak tightness specification is 2.5×10^{-9} mbar L s^{-1}.

Figure 3 presents the vessel flanging. The door is equipped with five DN200 and four KF40 flanges (Figure 3, left), while the body features one DN200 and four KF40 flanges on the side opposite of the door (Figure 3, right), four KF25 flanges and one KF40 flange on the left side of the body (Figure 3, middle), and four KF40 flanges on the right side. The KF25 and KF40 flanges are used for High Voltage (HV), gas, and vacuum system feed-throughs. The five DN200 flanges on the door are each equipped with a custom optical window flange and camera mount incorporating a 60 mm thick quartz optical window (Figure 4). The body flanges host two independent pressure relief systems. The first is a 5 barG burst disk that is backed by a 5 barG pressure relief valve. The second, on an independent body flange, is a 6 barG burst disk.

The interior of the vessel houses three steel rails that run longitudinally along the walls, which are separated at approximately 120° to allow for the mounting of equipment inside the chamber. The interior surfaces are shot blasted.

The vessel is rated to a 6 barA. To verify this after construction, the vessel was filled with water and subjected to the test pressure of 7.2 barG for 10 min. No evidence of leaks or material deformation was observed. The hydrostatic pressure was subsequently decreased to the working pressure of 5 bar absolute pressure and then maintained for 90 min in order to verify the tightness of the pressurized vessel. After the test, the vessel was emptied and dried with nitrogen gas. All of the optical windows were installed during

this test, which validated the design of the custom DN200 optical flanges. Given the 1472 L volume, the vessel is a category IV pressure vessel. This hydrostatic test was used to follow the conformity assessment procedure MAT-17-CE-G-CRTO02/17 in order to obtain the declaration of conformity with pressure vessel directive 97/23/CE.
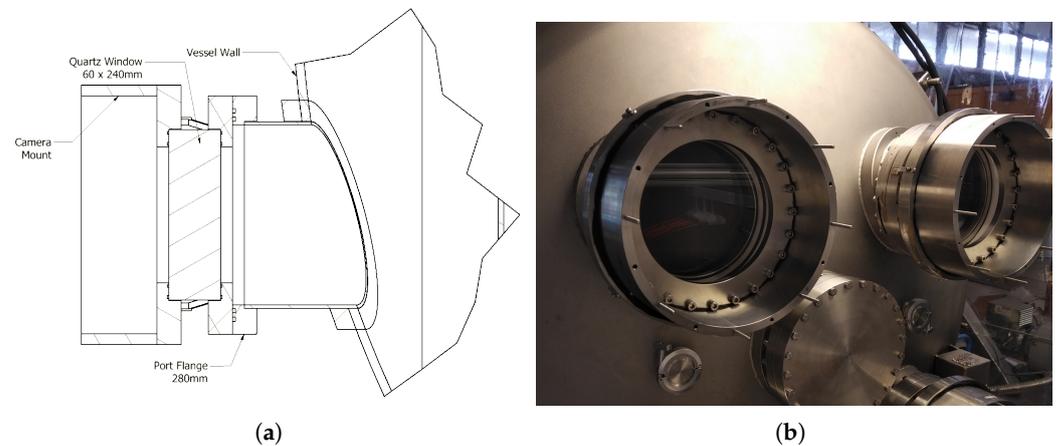

(**a**)　　　　　　　　　　　　　　　　　(**b**)

Figure 4. (**a**) Drawing of the optical flange with the camera mount. The thick quartz is necessary for ensuring that the assembly can withstand the pressure difference between the vessel pressure and ambient pressure. (**b**) A photograph of the assembly with the camera removed.

Gas System

Figure 5 shows the gas and evacuation system for the HPTPC prototype detector described here.
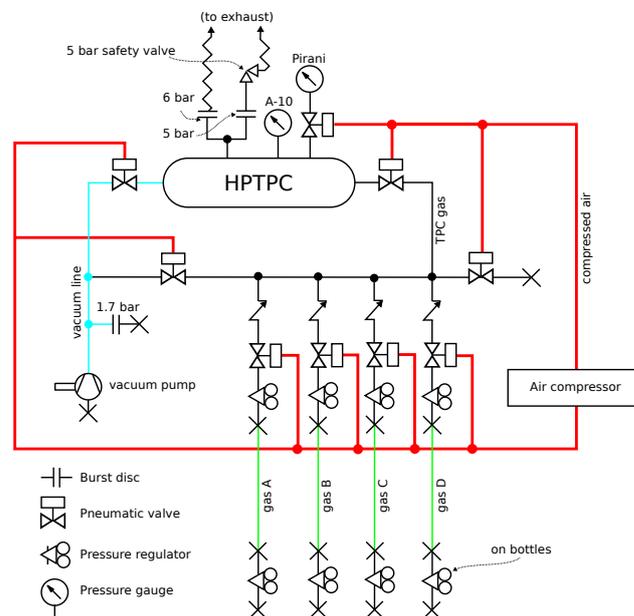

Figure 5. Diagram of the gas fill and evacuation system for the HPTPC vessel.

The gas filling strategy for the HPTPC foresees evacuating (and purging) the vessel prior to the target gas fill. An Agilent Triscroll 800 dry vacuum pump is used to pump the vessel down to a pressure of approximately 1×10^{-6} barA before gas operations. The same pump is used to evacuate the fill line from the gas system to the vessel with the purpose of reducing contamination, either during the filling procedure or in case a gas fill is topped up to a higher pressure. The system enables the mixing of gases from four different inputs, using eight Aura gas pressure regulators with manometers and threaded connections (four in the primary $200 - 10$ bar stage and four in the secondary $10 - 0$ bar

stage). The mixtures are achieved by filling with different gases in turn, while partial pressure adjusts the respective proportions. The lines from gas bottle to the gas system are purged using gas from the bottle whenever a new bottle is connected.

All of the valves can be opened and closed remotely using the slow control system. The system consists of eight 0.5 in Swagelok solenoid valves and one 1.5 in Carten solenoid valve, which are all pneumatically activated. The gas pressure is monitored by a Wika A-10 digital pressure gauge (from 0.8 barA to 6 barA absolute pressure), and by an Inficon PGC550 combined capacitance-Pirani vacuum gauge for pressures that are between 5×10^{-8} barA to just below atmospheric pressure. Because the Pirani gauge is not suitable for over-pressure, it is protected by an electronically controlled valve when the pressure exceeds 0.8 barA. The slow control system logs the gas pressure from the two gauges as well as the ambient laboratory temperature, being measured by a SynAccess TS-0300 sensor, for later use in the analysis.

4. Time Projection Chamber

The field cage and the electrodes that define the drift and amplification regions are the principal components of the time projection chamber. Figure 6 shows the field cage ring structure and the amplification region before the assembly is inserted into the pressure vessel (left), and in-situ—including the cathode—before the pressure vessel is closed (right).
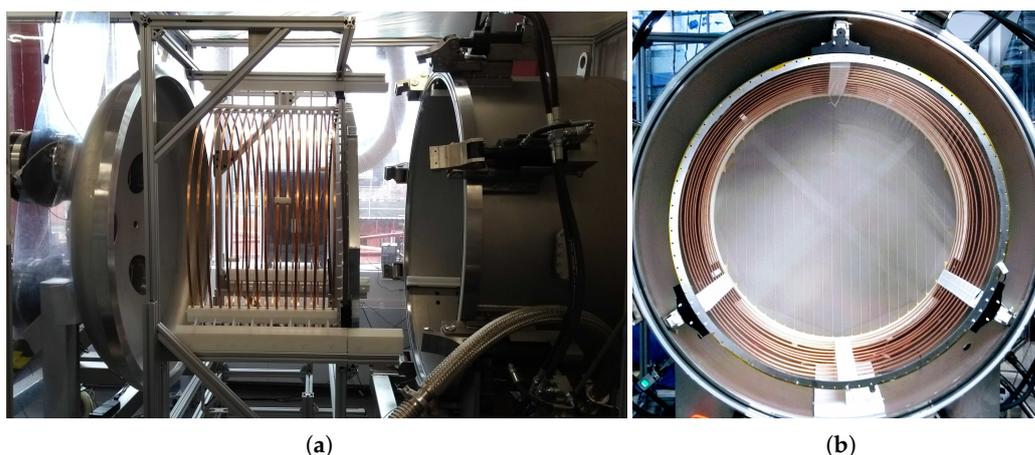

(**a**)　　　　　　　　　　　　　　　　　　　　　　　　(**b**)

Figure 6. (**a**) The field cage before insertion into the pressure vessel and (**b**) after insertion. The latter picture is photographed through the high-transparency cathode towards the amplification region and shows the full TPC.

4.1. Field Cage

The field cage (Figure 6a) is constructed of 12 copper rings with an inner diameter of 111 cm, and length of 1.0 cm in z and 0.6 cm in r. The distance between two neighbouring rings is 2.5 cm. Each ring is supplied with HV via the cathode in series with 3 MΩ resistors being held in place with compression fittings between subsequent rings. The last ring on the field cage facing the amplification region is connected to the ground via a resistor, where the value is chosen depending on the spacing between the final ring and the amplification region to maintain field uniformity. The total length of the field cage is 42.4 cm, whih results in a 44.7 cm drift distance between the cathode and amplification region.

The field cage assembly is supported from the three internal rails on the pressure vessel by machined Delrin parts. One set of these supports houses the resistor chain. The size of the support between the vessel rails and field cage is adjustable.

4.2. Cathode Electrode

The cathode is a 25 lpi (*lines per inch*) steel mesh made from 27 µm diameter wires. Because of its low wire density, the mesh has a calculated transparency of ~97 %, which allows for camera imaging of the amplification region through the cathode mesh (Figure 6b).

A 122 cm×122 cm square of this mesh was stretched to a tension of 6.4 N cm^{-1} on a Grünig G-STRETCH 210 mesh stretching machine. After stretching, the mesh was epoxied using DP460 epoxy to a circular stainless steel ring, with 118 cm outer diameter, 112 cm inner diameter, and 0.3 cm thickness.

The tension measurement employs a Teren Instruments HT-6510N tension meter; the measurements are made at nine points on the mesh. The average tension reported here is the average of measurements at these nine locations, after the stretching and relaxation procedure is completed. The standard deviation of repeated tension measurements across the nine spatial locations is measured to be $0.4 - 0.8$ N cm^{-1} [24].

Machined Delrin pieces support the cathode assembly on the three internal rails of the vessel. The spacing of the cathode to the first field cage ring is constrained by the Delrin supports of the cathode and the mating support parts of the closest field cage ring.

4.3. Gas Amplification Stage

The amplification stage is constructed from three electrodes (anodes), which are separated by two resistive spacers. The resistive spacers are 121 cm outer diameter, 112 cm inner diameter rings, with 24 wide beams, 0.1 cm each, crossing them, and being laser cut from polyester shim stock. The spacer beams are visible as the vertical lines in the anode plane seen in Figure 6b.

The amplification region flatness is constrained by its support frame, which consists of two ring-shaped frames that are made of Nylon bolted together, which sandwich the anodes and resistive separators. The frame dimensions are 118 cm outer diameter, 112 cm inner diameter, with a thickness of 1.6 cm. The two rings and each amplification mesh and resistive spacer ring have 88 aligning drilled holes. A stack is formed with one support frame on the bottom, followed by alternating the three amplification meshes with the two resistive spacers and finishing with the second support frame. Nylon bolts are passed through the 88 drilled holes in the stack. Finally, on the side facing away from the camera readout, a hexagonal aluminium stiffener is bolted to the framed assembly, which is then attached to the nylon bolts at 16 of the 88 drilled holes points.

The three anodes are constructed from steel meshes with 121 cm diameter. Anodes 1 and 2 are made from 100 lpi meshes with a wire diameter of 27 µm. The optical transparency of the anode 1 and 2 mesh is 89%. The third anode is made from a 250 lpi mesh with a 40 µm diameter. We chose the meshes with the smaller wire diameters for the two meshes that are closest to the field cage in order to achieve the highest gas amplification in the first stages and minimize the loss of light due to imaging the amplification region through the cathode, anode 1, and anode 2 meshes. The meshes are epoxied to stainless steel rings (outer diameter 118 cm, inner-diameter 112 cm, and thickness 0.1 cm) after stretching the meshes, as described for the cathode. The procedure for stretching the anode meshes takes approximately one week of successive stretching and relaxation of the mesh. Following this procedure, the average tension force on the anode 1 and 2 meshes is 16.8 N cm^{-1}. The measured tension is uniform over the plane of the anode mesh to be better than 5 %. The average tension force on the anode 3 mesh is 38 N cm^{-1}. After stretching, the meshes are epoxied to the stainless steel support ring in the same way that has been described for the cathode [24]. The goal for the distance between the anode 1 and anode 2 (anode 2 and anode 3) meshes is 0.5 mm (1 mm). Section 6.3.1 describes a measurement of the capacitance of the amplification region. The capacitance measurement implies that the distances achieved were approximately 1 mm (2 mm) spacing. This is likely due to the epoxy and spacer thickness tolerances as well as flatness variation.

Like the cathode, the amplification region assembly is supported on the three internal rails on the pressure vessel while using machined Delrin parts. These supports constrain the amplification region distance to the closest field cage ring.

4.4. High-Voltage Distribution System

The anode meshes are provided with positive HV by either a CAEN NDT1470 or a CAEN N1470 multi-channel Power Supply (PS), which is controlled through a serial link over USB. The cathode power supply is a Spellman SL 30 PS with a maximal output voltage of 30 kV. The resulting limit on the electric field in the field cage is over $600 \, \mathrm{V \, cm^{-1}}$. The cathode PS voltage is controlled by varying an analogue input from 0 to 10 V, which results in an output voltage from the PS of 0 V up to its maximum voltage. This analogue signal is generated by the slow control system using a LabJack U3-HV USB Data AcQuisition (DAQ) device that is connected to the Spellman PS control input.

The various meshes are connected to the power supplies through the following chain: inside the pressure vessel, all meshes are connected to Kapton coated copper wires, which, in turn, are connected to the HV feed-throughs that pass through the pressure vessel wall. In order to provide extra insulation, these wires have ceramic beads that are threaded along their entire length, and a fibreglass sheath also surrounds the resulting assembly. In the case of the anodes, the HV feed-throughs are rated to 10 kV; in the case of the cathode, the feed-through is rated to 20 kV. Outside the pressure vessel, each anode's feed-through connects to a custom *bias box* via coaxial cables. These bias boxes decouple the charge signals from the constant current HV, as shown in Figure 7. Therefore, each bias box connects to the respective PS and each box has a signal output that is fed into the TPCs charge readout system. The signals are routed from these signal-outputs through a preamplifier, as described in Section 4.5. The RC constant of the R_{in} resistor and respective mesh capacitance of $\sim$5 nF, as well as the RC constant of the filter circuit, limit the charge-up speed of the meshes and, in turn, help to quench discharges. The output from these preamplifiers is fed into the detector's DAQ system, which is described in Section 4.7.

The cathode feed-through is connected to a coaxial power supply cable using a custom Delrin assembly that separates the grounded outer conductor of the cable from the voltage carrying inner conductor. The grounds of the power supplies (both anode and cathode) are connected together in a grounding circuit that is coupled to the pressure vessel.

The voltages and currents that are supplied by each power supply channel are recorded by the detector's slow control system for use in later analysis.
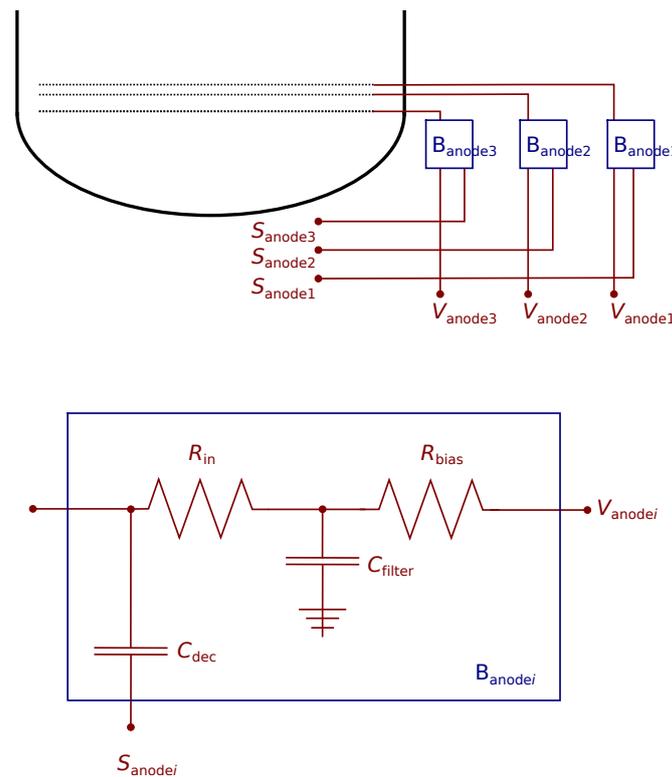
Figure 7. Schematic of the circuit to bring high voltage ($V_{\text{anode}i}$, $i \in 1, 2, 3$) to the anode meshes and decouple the signal from the high voltage lines. The signals are decoupled in bias boxes via a 10 nF decoupling capacitor (C_{dec}) and are then fed to the signal line ($S_{\text{anode}i}$). These bias boxes $B_{\text{anode}i}$ also feature a protection and filtering circuit consisting of a bias resistor ($R_{\text{bias}} = 200\,\text{M}\Omega$), filter capacitor ($C_{\text{filter}} = 10\,\text{nF}$), and input resistor at the detector input ($R_{\text{in}} = 10\,\text{M}\Omega$).

4.5. Charge Signal Measurement

The pre-amplifiers that are used for the detector's charge readout are charge-sensitive CREMAT CR-113 (or CR-112) hosted in CR-150-R5 evaluation boards. The specified gains of the pre-amplifiers are $1.3\,\text{mV}\,\text{pC}^{-1}$ (or $13\,\text{mV}\,\text{pC}^{-1}$, respectively). Section 6.3.1 presents a measurement of the agreement of our preamplifiers with this value. The output signals from the preamplifiers are digitized by a CAEN N6730 8-channel digitizer, with 2 V dynamic range and 500 MHz sampling frequency.

4.6. Optical Signal Measurement

The optical readout system uses four FLI Proline PL09000 CCDs, each of which contain a front-illuminated Kodak KAF-09000 chip with 3056×3056 active pixels (9.3 Mp) and a pixel size of $12 \times 12\,\mu\text{m}^2$. The chip has a Quantum Efficiency (QE) in the range of 50–70% for photons with a wavelength between 475 nm and 750 nm. In the wavelength range from 350 nm to 925 nm, the QE is always larger than 20%. These wavelength ranges cover the full VIS part of a spectrum and extend towards the NIR and UV, which makes the TPC sensitive in the regions of the spectrum discussed in Section 2.

Each camera's field of view is centered on a quadrant of the amplification plane. Each camera is coupled to a Nikon f/1.2, 50 mm focal length lens with a 54.8° angle of view. The cameras are mounted to optical flanges, as shown in Figure 4. Quartz windows of 6 cm thickness are used to allow the desired overpressure in the vessel. The transmission of the optical flanges is measured to be $97^{+3}_{-4}\%$ for red light. The camera lenses have a transmission of 70% (90%) at 420 nm (750 nm) wavelengths, where the lens transmission includes all of the photons lost between the seven elements of this compound lens.

When adding TPC drift distance, the non-active area between the cathode and vessel door, as well as the path through the camera assembly, the total object distance is approximately 102 cm, which is larger than the minimum focal distance of our camera lenses. At this distance, the system images a 71×71 cm field of view with a vixel side length (pixel width in the amplification plane) of $\sim$40 µm, when no extra readout binning is applied. When considering the full optical path, including quartz window and lens, we estimate a geometric acceptance of the optical system—the third term in brackets seen in Equation (1)—of approximately 1.1×10^{-4}. Achieving a high enough gain in the amplification region to produce enough photons for signals to be detected above the noise, when considering this acceptance, is key.

The CCDs are cooled to $-25\,^{\circ}\text{C}$ to $-30\,^{\circ}\text{C}$ to achieve optimal noise performance. The cameras are equipped with an internal thermoelectric cooler that can cool the CCD to approximately $50\,^{\circ}\text{C}$ below the ambient camera temperature. This is supplemented by a water cooling system attached to each camera to reduce its ambient temperature by $15\,^{\circ}\text{C}$. At $-25\,^{\circ}\text{C}$ operating temperature, the read noise per pixel is in the range of 9.6 to $11.3\,\text{e}^-$ and the dark rate is $0.006 - 0.025\,\text{e}^-/\text{pixel/s}$ (the range of variation is across the four cameras).

The CCDs digitize the number of electrons collected in each pixel in each exposure. For scale, the typical conversion gains of the cameras are $1.52 - 1.55\,\text{e}^-/\text{ADU}$, where ADU stands for *analogue-to-digital units*. Pixels are grouped prior to digitization to mitigate the dominant effect of readout noise. This grouping reduces the noise per pixel in the group by approximately $1/\sqrt{N_{\text{pixels}}}$ given the relative scales of readout noise and dark current rate in a 1 s exposure. We typically use 8×8 groupings ($N_{\text{pixels}} = 64$), as this gives an acceptable balance between readout noise and readout pixel size, with the effective vixel side length being approximately 2 mm.

4.7. Slow Control

The slow control software sets and monitors the detector voltages, gas pressure, and ambient temperature. The software has a web based user interface, and it uses java and C++ software to interface with an SQL database. The database contains the values of the monitored variables as well as the desired set points for these variables. The detector control code reads the set points from this database and communicates with the high voltage power supplies to set the required voltage and read out the measured voltage and current into the database. The same web interface also achieves control of the gas system, which is able to launch code communicating with the valve control hardware to automatically perform filling, venting, and evacuation.

4.8. Data Acquisition

The DAQ system triggers and acquires data from the charge and optical readout hardware. The DAQ commands are sent from the same web interface that is used for slow control to a DAQ PC that communicates with the cameras and CAEN N6730 digitizer used for the charge signals to initiate each run. A run consists of a user-specified number of camera exposures (data frames), which are simultaneously acquired from the four cameras as well as the charge waveforms digitized during the exposure time. Additionally, at the start of the run, a specified number of frames are acquired while the camera shutters are closed. The use of these frames is to subtract off the baseline behavior of each pixel in the CCD chip when it is not exposed to light (Section 5.2). After these empty frames, the data frames are taken with the camera shutter open. The detector can run in two triggering modes. In the first mode, the data frames are taken immediately after each other, being separated only by the CCD readout time. In the second mode, the data frames are taken based on an external trigger signal. During the CCD exposure time, the charge waveform digitizer (see Section 4.5) is triggered by signals that are larger or smaller than a user-configurable threshold amount above or below the baseline on each channel, and then records waveforms of typical duration 200 µs around each trigger, including a configurable

period of time before the trigger event. The digitizer can also be triggered externally. In both triggering modes, any trigger causes all eight channels of the digitizer to be read out simultaneously. The DAQ system stores the configuration of all the parameters described in this subsection for each run.

5. Optical Readout Analysis and Performance

In this section, we report on the results of data taking with ^{241}Am sources mounted in the pressure vessel. The HPTPC was also tested using a beam at CERN, the analysis of which is ongoing and not presented here. After explaining the CCD calibration (Sections 5.1 and 5.2), we show a first scan of various gas mixtures (Section 5.3) to establish the most promising mixture for a more comprehensive light gain measurement. Section 5.4 then shows this in-depth measurement with a single mixture and its analysis.

Am-241 predominantly emits either a 5.486 MeV (84.8%) or 5.443 MeV (13.1%) alpha particle (α) and different energy gamma-rays (γ), where the most probable ones have an energy of 59.54 keV or 26.34 keV [25]. Furthermore, there is a substantial amount of X-ray radiation in the range from 10 keV to ~20 keV. The α particles pass through a foil before they enter the gas volume; therefore, their energy is reduced by approximately 860 keV to ~4.56 MeV [26]. Such α particles are stopped inside the gas volume and they deposit their full remaining energy. The γ-rays have high enough energy to escape the active TPC volume. Only 1.2% of all γ-rays interact in the counting gas, according to a HEED [27] and GARFIELD++ [28] simulation that takes the HPTPC's geometry into account. The lower energy X-rays are more likely to interact; we find that 58% are absorbed in the active gas volume when integrating over all X-ray energies. Their overall contribution is still not large, since the ratio of the X-ray count over γ-ray count is approximately 12%. The emission distribution of the ^{241}Am in the forward hemisphere is roughly isotropic for the different kinds of radiation. Furthermore, there is a contribution from the cosmic rays.

Figure 8 shows the result of a HEED and GARFIELD++ simulation of the expected energy deposits by these different sources of radiation, which does not take any trigger effects, electronic noise, gas gain, or an amplifier response into account. For the simulation, we assume a quadrant of the HPTPC's volume with a source location that is similar to the location in the experiment. The normalization of the three different kinds of radiation preseted in Figure 8 is given by the result of the simulation: For 1000 Bq of ^{241}Am decays, all 1000 α particles interact in the active volume every second, as do 70 X-rays and γ-rays. Note that the X-rays and γ-rays only contribute at the low energy end of the spectrum. The contribution from the cosmic rays per second is scaled up by a factor of 60 to make the shape of the cosmic ray spectrum more visible. The most distinct feature of the spectrum is the α-peak from the ^{241}Am decay at ~175×10^3 electrons. It turned out to be not feasible to simulate stopping of α particles with ~5 MeV in HEED + GARFIELD++. Therefore, we ultimately simulated 11.8 MeV α particles, evaluated their most probable energy loss, and scaled this energy loss to 4.56 MeV. For a gas pressure of 1 atm, these ionizations are created along a 5 cm to 10 cm long trajectory, yielding a high ionization density along the track. For larger pressures, the track length decreases and the ionization density increases. When amplified, this high ionization density will result in many photons being produced in a small area. Thus, an α particles' energy deposit in the detector is more easy to image with cameras than less ionizing forms of radiation. Furthermore, a gain measurement is possible, since the total energy that is deposited in the detector is known.
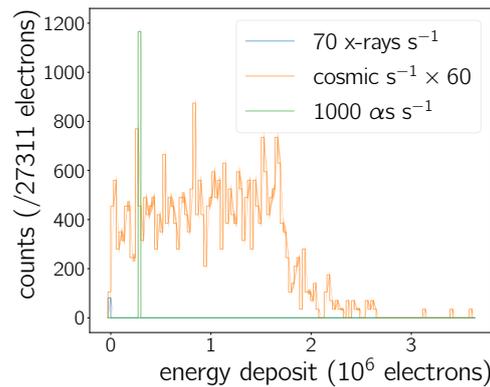
Figure 8. The simulated energy deposits of ^{241}Am decay radiation and cosmic muons inside a gas volume filled with Ar/CO_2 (90/10). Energy deposits are measured in the number of liberated electrons during the energy deposit. This is the result of a HEED [27] and GARFIELD++ [28] study taking the approximate layout of the HPTPC and the information in [25,26] into account.

In the amplitude spectrum of the charge readout (*cf.* Section 6.3.2), we expect to see something that is qualitatively similar to the spectrum shown in Figure 8. However, the simulation does not take the energy resolution of the amplification plane into account; hence, the actual measured quantity—amplitudes or light intensity—will exhibit a spread larger than what is shown in the plot. Furthermore, electronic noise is not included, which is a substantial contribution at threshold.

Two different configurations were used in our measurements: one using five ^{241}Am sources and one using a single ^{241}Am source. In the single source configuration, the source is either visible in the overlap region of the top two cameras or the bottom two cameras. In the five source configuration, the sources are arranged in a cross configuration and they are distributed so that there are always two sources in the overlap region of two cameras and the central source can be seen by all cameras. Occasional sparks can be used to map these positions in the recorded frames (Figure 9a).
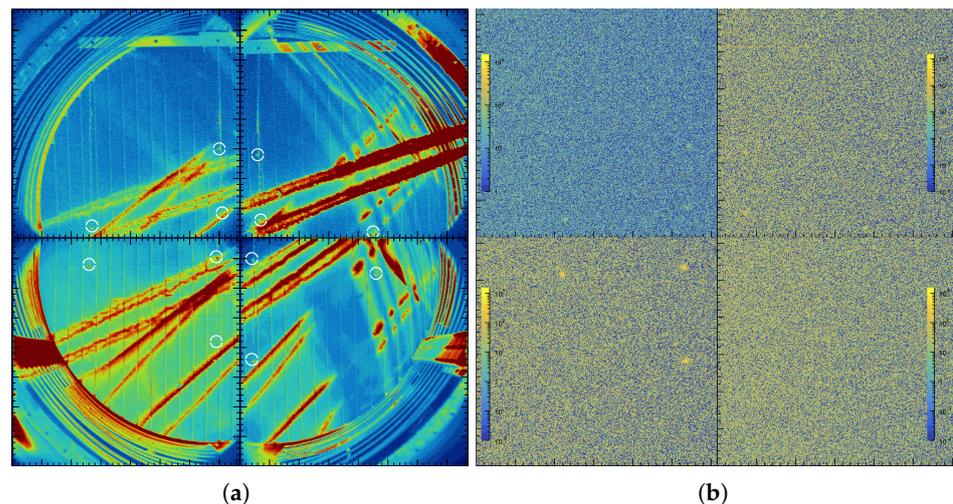

(**a**)   (**b**)

Figure 9. CCD images showing the readout plane of the HPTPC; the vertical (horizontal) image axis points along the y (x) direction. The color encodes the light intensity in arbitrary units. (**a**) Simultaneously recorded frames during a spark event. The locations of the ^{241}Am sources (marked by circles) inside the TPC are visible during the spark event as well as the field cage rings and the anode support, *cf.* Figure 6b. (**b**) The light yield from the calibration sources for 200 s exposure time in pure Argon at 3 bar absolute pressure. The intensity of the image in the top left frame differs from the other three frames, because the corresponding camera has a different conversion gain.

5.1. Spark Detection

A major source of noise comes from sparking in the chamber. These sparks mostly originated along the boltholes of the amplification region and from the cathode feedthrough. The frequency of these events increased with the anode and cathode voltages, and ultimately limited the maximum voltages that we were able to reach. Thus, our gas mixture choices were driven by finding mixtures that allowed for operating the detector without many discharges at large enough voltages to see charge and light signals. The gas mixtures that are listed in Section 5.3 allowed us to operate the detector in a stable manner. Other gas mixtures, such as Ar/CF_4, were also tried during the initial testing, but they resulted in too many discharges to perform a light gain measurement and, hence, are not reported on.

Sparks cause a large fraction of pixels in an image to become significantly brighter; Figure 9a presents a particular drastic example. The camera pixels measure charge in ADU. Images with sparking are rejected from the analysis, as follows. First, events in which one of the CCD images has a pixel-value RMS above ∼100 ADU to 300 ADU are rejected as sparks. Of the remaining images, those with events in which one or more of the CCD images have 100,000 pixels above 100,000 ADU are also removed from the analysis. The exact thresholds depend on the actual CCD camera and detector settings, e.g., the RMS thresholds vary from 133 ADU to 300 ADU between the four cameras. The exact values for each threshold have been identified by comparing the properties of the spark images that are selected by eye to images without sparks.

5.2. CCD Camera Calibration

The CCD camera calibration removes variations in pixel gain, transient phenomena, and time dependent noise sources. The subtraction of *bias frames* is the first step of the CCD calibration, which deals with persistent features and noise sources, and accounts for variations in pixel gain. At the start of each run, we take 5–10 bias frames with the shutter closed. These are averaged and then subtracted from all *exposure frames* with the shutter open in the same run, where a typical run consists of 20–100 images (per camera) with an exposure time of 2 s per frame.

A source of transient noise is *hot pixels*, which are created e.g., by cosmic muons passing through the camera chip and saturating pixels. These hot pixels are usually confined to individual frames, but they can remain saturated over several exposure lengths. If they occur in the bias frames, they must be corrected before the bias frame subtraction from the exposure frames. Each pixel value of each bias frame is compared to the values of the same pixel in the other bias frames, and the value of the pixel is set to that of the previous bias frame if its ADU reading has changed by more than five standard deviations of its mean ADU value in that run.

The temperature dependent image mean correction is the next step of the CCD calibration. The temperature of the CCDs is seen to increase with the number of events taken in a run. This results in a natural upwards drift in the pixels' intensities with time, which contributes to the noise. This effect is corrected for by calculating each CCD frame's average pixel value, and then subtracting that value from every pixel within that frame. This process is applied to every frame in all runs.

The reduction of pixel intensity variance is the impact of these calibration steps. Figure 10 shows the distribution of pixel values before and after bias subtraction.
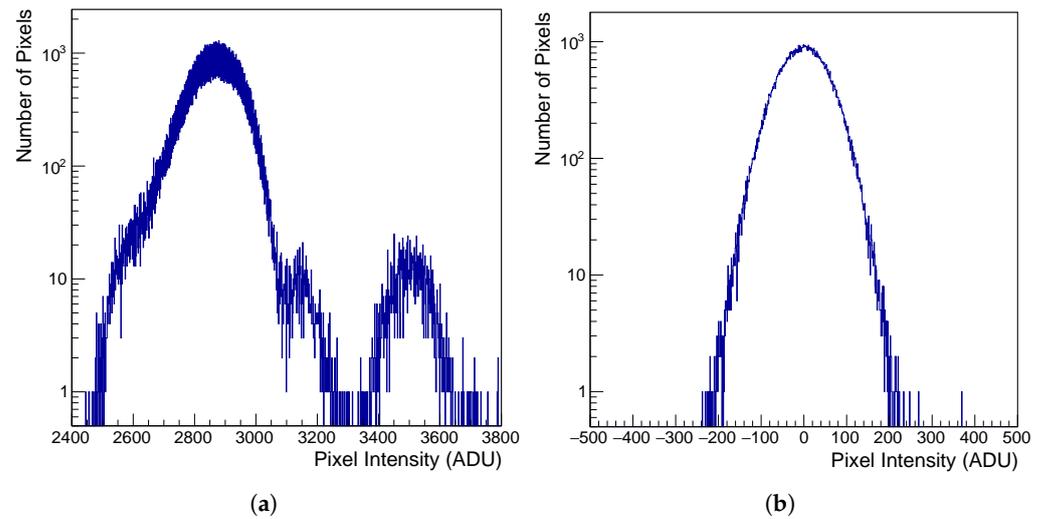
Figure 10. Analogue-to-Digital Unit (ADU) distribution of all pixels of an exposure frame before (**a**) and after (**b**) bias subtraction.

5.2.1. Calibration without Closed-Shutter bias Frames

The measurements shown in this paper are grouped into two data taking periods: firstly, where we explore different gas mixtures to find the most promising gas for an in depth measurement campaign (Section 5.3), and the second period, where only the gas identified in the first period is studied (Section 5.4). During the beginning of the second period, it was discovered that camera 2 (which was set up to take the light gain data) had a stuck open shutter. Because of time constraints, we continued with data taking despite this and have adjusted our calibration accordingly, as detailed in this section.

A procedure was developed to acquire bias frames for calibration with the shutter open in order to address mechanical shutter failure. To avoid stray light from the sources or sparks, 1000 2 s shutter-open frames were acquired daily with the TPC voltages being switched off. The anode meshes need to be slowly brought up to the desired voltages in order to reduce the probability of sparking and the subsequent need to reduce the voltages for some time. Thus, reaching the target voltages in a gas mixture with low or no quencher content can take a number of hours, when starting from zero. For this reason, we decided to not take these shutter-open bias frames before every run. These frames are then used to produce a single, low noise *super bias* frame to be subtracted from each event taken that same day.

5.2.2. Super bias Frame Creation

The method used to create each super bias is to first remove any anomalous pixels by the method that is described in Section 5.2. Next, a one-dimensional (1D) distribution for each pixel in the super bias is created and filled with the $N_{\text{bias}} = 1000$ ADU values being measured by that pixel in all 1000 bias frames. The mean and standard deviation (σ_{pixel}) of that distribution are calculated, and any ADU values above $3\,\sigma_{\text{pixel}}$ of the mean are removed. A Gaussian is fitted to the remaining 1D distribution of each pixel. The centre of the Gaussian gives the ADU value of that pixel in the super bias. Bias subtraction using a bias frame, taken close in time to the event frame, can help to reduce temperature (and, therefore, time) dependent noise. Because of the significant time difference between bias and event frames, additional corrections of temperature/time dependent effects need to be implemented before the super bias frame can be used as a bias frame for exposure frames.

Figure 11a shows an example of the row pedestal artefacts. The scale of the effect has been artificially increased for demonstration purposes by using exposure and bias frames that were taken days apart. This effect occurs when the pedestal of each pixel within a row changes by some amount between taking the bias and exposure frame. These effects are

not observed when the bias frames are directly recorded before the exposure frames as part of the same run, since the pedestal value shift only occurs between runs. We apply a row correction to every row in the super bias subtracted image in order to use the super bias frames. For this correction, the average ADU value of a row is calculated whilst omitting any anomalous pixels or any pixels that are located within the region of interest for the analysis, i.e., the source locations. This average is then subtracted from each pixel in that row. Figure 11a shows the same image as Figure 11b after row correction has been applied.
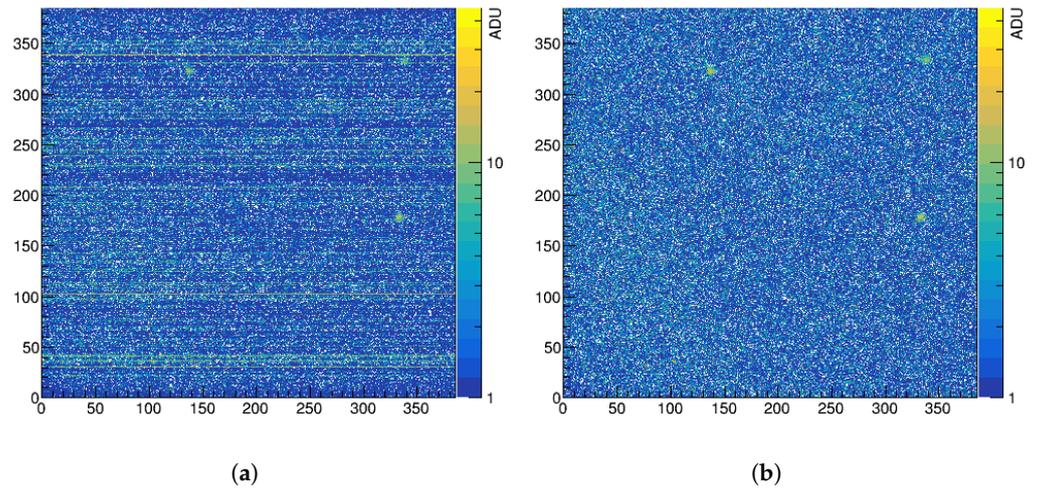

(**a**)   (**b**)

Figure 11. Example of the average of 100 bias subtracted events with event and bias frame taken days apart (**a**) before row correction (demonstrating row CCD artefacts) (**b**) after row correction (demonstration correction of row CCD artefacts). The colour in both plots encodes the ADU value at the position of a pixel, while the horizontal and vertical axis shows the y and x coordinate, respectively.

Applying row correction to a super bias subtracted image also corrects for any time dependent drift of pixel intensities (e.g., because of temperature). Figure 12 shows an example of the pedestal drift in 100 subsequent exposures (events) for 150 different runs before and after row correction. The bi-modal nature of Figure 12a is likely due to temperature differences on different days. It should be noted that the row correction can fail for regions on the CCD where a differential pedestal drift is present. The lower left corner of the CCDs experiences such a non-differential shift and care has been taken to ensure that the source positions do not overlap with affected rows.

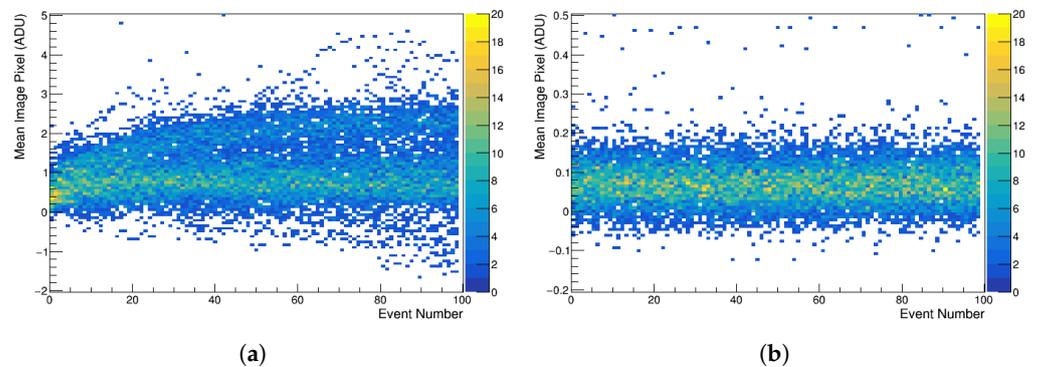(**a**)   (**b**)

Figure 12. Mean ADU value of exposure frames versus event number for 150 runs (of 100 events, i.e., frames) taken over a number of days (**a**) before row correction (demonstrating pixel pedestal drift) (**b**) after row correction. The latter demonstrates the correction of the pedestal drift by the row correction procedure.

Overall, super bias frame subtraction significantly reduces the pixel intensity variance in an event that is normally introduced by the classical bias frame subtraction, because the mean pixel value error in a super bias frame is reduced by $1/\sqrt{N_{\text{frames}}}$. When integrating a region of interest of 9×9 pixels, i.e., $N_{\text{pixel}} = 81$, this 100% correlated uncertainty for a super bias frame that is constructed from 1000 (bias) frames ($N_{\text{bias}} = 1000$) can be calculated while using the following equation:

$$\sigma_{\text{bias}} = \sqrt{\frac{\sigma_{\text{pixel}}^2 \cdot N_{\text{pixel}}}{N_{\text{bias}}}} \quad . \tag{3}$$

For the standard deviation of a single pixel (σ_{pixel}), a typical value of 40 ADU can be used to estimate σ_{bias}. The resulting $\sigma_{\text{bias}} = 11.4$ ADU is significantly smaller for e.g., the case where five bias frames are used.

5.3. Light Yields for Different Gas Mixes

Which gas mixtures will yield the most light from the interactions of interest is an important question when operating gaseous detectors with optical readout. For this measurement, light from a single ^{241}Am source in the overlap region of the top two cameras was used. Because the alpha particles from the decays only travel a few cm at the pressures considered (*cf.* the beginning of the section), a small region around the source location was considered for the light yield measurement. One of the cameras (top left, Figure 9b) had a lower conversion gain than the other three, so only the top right camera was used for this analysis. The trialled gas mixes were: pure argon (3 and 4 bar absolute), argon with carbon dioxide (4 bar absolute, Ar/CO_2 (99/1) and (99.25/0.75)), argon with nitrogen (3 bar absolute, Ar/N_2 (98/2)), and argon with nitrogen and carbon dioxide (4 bar absolute $Ar/CO_2/N_2$ (98.75/0.75/0.50) and 4.9 bar absolute $Ar/CO_2/N_2$ (96/2/2)).

The calibration procedures shown in Sections 5.1 and 5.2 are applied to the relevant data runs in order to determine the light gain. A 20×20 pixels ($\sim 3.8 \times 3.8\,\text{cm}^2$) region of interest around the source position is examined in the bias subtracted and calibrated exposure frames. All of the light recorded in the region of interest is integrated. The results of this study can be seen in Figure 13. One data taking run has been used for each result presented in the two plots of Figure 13. All of the data are normalized to the same integrated exposure time.

Two different comparisons were made, one at fixed anode voltages (Figure 13a) and one at the maximum anode voltages that were reached during stable operation (Figure 13b). Table 1 shows the voltage settings for both data sets. In both cases, the light yield from the ^{241}Am source was found to be the highest in pure argon. The pure argon results also show that a high relative light gain can be achieved with lower voltages when compared to the gas mixtures with a quencher. The high light gain of the 4 bar pure argon measurement seen in Figure 13b is surprising, since a lower light gain than for the 3 bar gas mixture would have been intuitively expected. Even more so, as the voltages (normalized by pressure) thata re applied during the 4 bar measurement are lower than in the 3 bar case. A saturation of the light gain at a given voltage setting can explain such findings. Furthermore, the fields during the 4 bar measurements could allow for the incoming and amplified electrons to create more excitations and, thus, photons at the cost of ionizations, as compared to the 3 bar case.
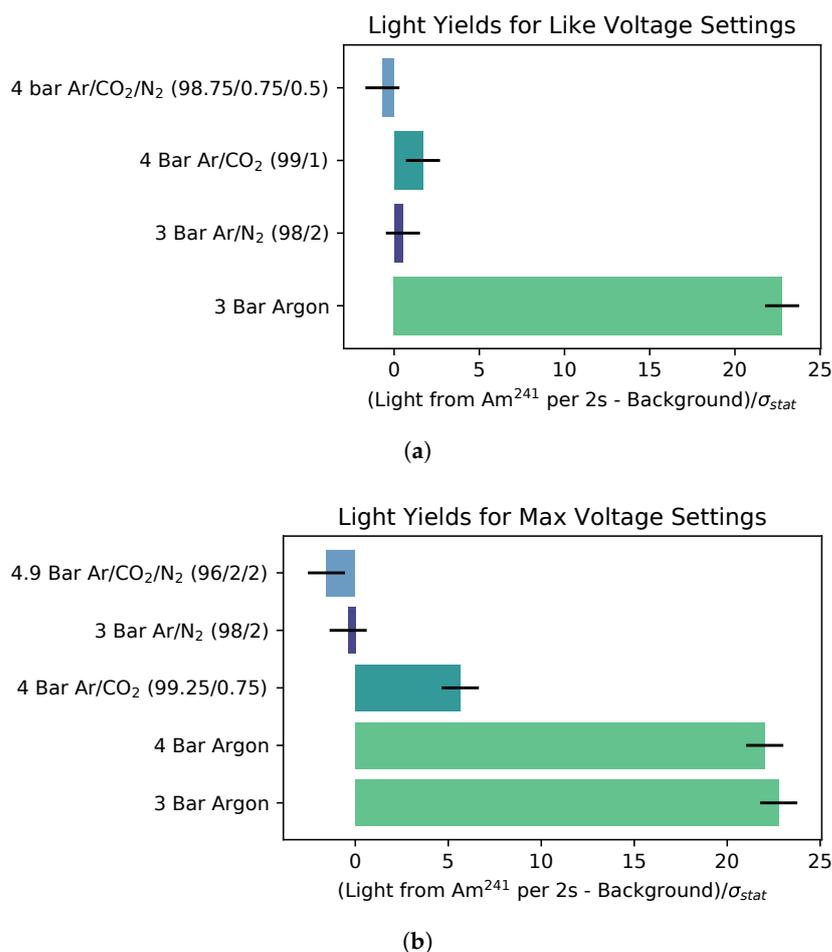
(**a**)

(**b**)

Figure 13. Light yield measured for an ^{241}Am source with different gas mixtures (**a**) at near constant anode and cathode voltages and (**b**) the maximal light yield achieved. Table 1 lists the voltages used during these measurements.

Table 1. Voltage settings for the result plot shown in Figure 13: the **top** table shows the voltages used for the settings that are shown in Figure 13a, while the **bottom** table shows the settings used for the data shown in Figure 13b. The absolute pressure is quoted.

mixture or gas	P	V_{a1} [V]	V_{a2} [V]	V_{a3} [V]	V_c [V]
$Ar/CO_2/N_2$ (98.75/0.75/0.5)	4 bar	1000	2000	4000	−7000
Ar/CO_2 (99/1)	4 bar	1200	2400	4000	−7000
Ar/N_2 (98/2)	3 bar	1200	2800	4000	−7000
Ar	3 bar	1500	2100	4500	−5250
mixture or gas	P	V_{a1} [V]	V_{a2} [V]	V_{a3} [V]	V_c [V]
$Ar/CO_2/N_2$ (96/2/2)	4.9 bar	3000	5900	7600	−8500
Ar/N_2 (98/2)	3 bar	1550	3300	5000	−5000
Ar/CO_2 (99.25/0.75)	4 bar	1200	2500	4800	−7000
Ar	4 bar	1000	1750	2800	−5700
Ar	3 bar	1500	2100	4500	−5250

5.4. Light Yield in Argon at Various Voltage Settings

Having identified pure argon as the brightest gas among the mixtures tested before, we now examine how the operational settings of our amplification stage affect the optical gain in this gas. In doing so, we use pure argon at a pressure of 3 bar absolute, following the findings outlined in the previous section. Precisely how each of of the multiple anodes contribute to the gain depends—among other parameters, such as e.g., the voltage

settings—on the anode's relative alignment, which, for meshes, is difficult to analytically and numerically model. The aim of the optical gain measurements in this section is to understand how the light gain of the TPC is affected by: (**a**) the absolute voltage of the three anode meshes V_{a1}, V_{a2}, and V_{a3} when the potential difference between meshes is kept constant; (**b**) the potential difference between anode meshes 2 and 3 (ΔV_{a23}); and, (**c**) the potential difference between anode meshes 2 and 1 (ΔV_{a12}). To do this, we chose three voltage schemes, which are as follows:

- Scheme A—Constant ΔV_{a12} and constant ΔV_{a23};

- Scheme B—Constant ΔV_{a12} and varied ΔV_{a23};

- Scheme C—Varied ΔV_{a12} and constant ΔV_{a23}.

A single ^{241}Am source is used to conduct a light measurement, which is positioned so that it can be imaged by camera 2, the bottom left camera. The source has an activity of 10 ± 1 kBq, as has been determined by an independent measurement, which was validated using ^{241}Am sources with known decay rates. An exposure time of 2 s per frame was chosen to balance the reduction of readout noise with a reduction in dead time due to lost frames from sparking.

5.4.1. Optical Gain Analysis

Schemes A, B, and C consist, respectively, of five, 11, and nine integrated ADU measurements taken at different anode voltage configurations with step-sizes of 200 V or 400 V. Each voltage configuration has between 1000 and 1500 events with one frame per camera each. Four sets of 1000 TPC-off shutter open bias frames were also taken to produce four super bias frames. One that was taken before Scheme A and then one taken after each of the three schemes. First, the calibrations and checks that are detailed in Sections 5.1 and 5.2.1 are applied. In doing so, all of the exposure frames recorded within one voltage scheme are independently subtracted with the super bias frame taken before and after the respective scheme. The more suitable super bias frame is selected for each scheme based on the Gaussian nature of the pixels' ADU distribution and the flatness of the x and y projections of the ADU distribution of frames within a scheme. Two super bias frames were selected, which resulted in Schemes B and C sharing the same super bias frame.

Subsequently, a region of interest around the source is defined (referred to as *source box*). The source box's size is optimized to contain as few pixels as possible whilst not rejecting any signal. The analysis found a nine by nine pixels ($16.56 \times 16.56 \text{ mm}^2$) source box to be optimal. After a loose pixel ADU cut, a Gaussian is fitted to the ADU values of the $N_{\text{pixel}} = 81$ pixels in the box for a given frame (as shown in Figure 14). The integrated ADU per frame is then calculated by: $I_{\text{frame}} = \hat{\mu}_{\text{pixel}} \cdot N_{\text{pixel}}$, where $\hat{\mu}_{\text{pixel}}$ is the mean of the fitted Gaussian.
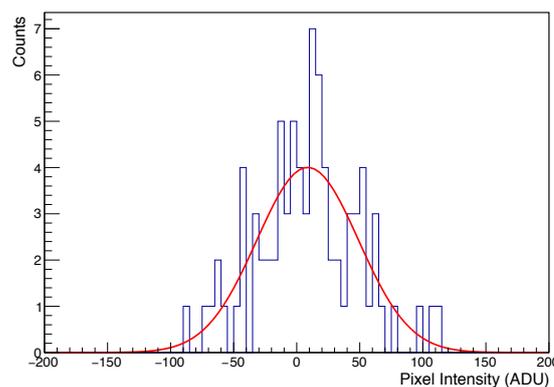

Figure 14. The intensity distribution of pixels within the source box for a single event.

The integrated ADU measurement for a run (I_{run}) is calculated by fitting a Gaussian to the distribution of I_{frame} values in that run. I_{run} is given by the mean of the fit and its uncertainty ($\sigma_{I_{\text{run}}}$) by the standard deviation on that mean. The final step takes the I_{run} values of the 10 to 15 runs in each configuration and then calculates their weighted mean ($\bar{I}_w$) and weighted standard error (σ_w). The mean and standard error for each voltage configuration are weighted by $w_i = 1/\sigma_i^2$, where σ_i is the standard deviation per run ($\sigma_{I_{\text{run}}}$) of the ith run in the configuration. The weighted mean and weighted standard error are calculated, as follows:

$$\bar{I}_w = \frac{\sum_{i=1}^{N_{\text{run}}} w_i I_i}{\sum_{i=1}^{N_{\text{run}}} w_i} \tag{4}$$

$$\sigma_w^{\text{m}} = \frac{\sigma_w}{\sqrt{N_{\text{run}}}} = \sqrt{\frac{\sum_{i=1}^{N_{\text{run}}} (I_i - \bar{I}_w)^2}{(N_{\text{run}} - 1) \sum_{i=1}^{N_{\text{run}}} w_i}} \tag{5}$$

where I_i is the integrated ADU value per run (I_{run}) of the ith run in the configuration, N_{run} is the total number of runs in the configuration, and σ_w is the weighted standard deviation. $\bar{I}_w$ and σ_w^{m} provide the final integrated ADU value of the voltage configuration (I_{config}) and its uncertainty ($\sigma_{I_{config}}$). In theory, one could calculate $\sigma_{I_{config}}$ without the intermediate step of calculating I_{run}. However, examining I_{run} ensures that the run-to-run instabilities are accounted for in the uncertainty of the final measurement.

5.4.2. Light Gain as Function of Voltage

Figure 15 presents the final results of the light gain measurements. In Scheme A, as shown in Figure 15a, the potential differences between the three anode meshes are held constant at 1200 V, while the voltages of all three are varied in 200 V steps. Scheme A is consistent with the light gain having no dependence on the absolute voltage of the three anodes while ΔV_{a12} and ΔV_{a23} are fixed at 1200 V, which suggests that the amplification is driven by the voltage differences between the anode meshes. Across all Scheme B voltage configurations, as shown in Figure 15b, $V_{a1} = 1200$ V and $V_{a2} = 2400$ V, respectively, while V_{a3} and, thus, ΔV_{a23}, are varied. Scheme B shows a clear linear dependence of light gain on ΔV_{a23} over the range 0 V to 2500 V with a gradient of 0.074 ± 0.005 ADU/V ($1.50 \pm 0.01 \times 10^{-2}$ ADU/(V/cm)). Across all of Scheme C (Figure 15c), the voltage configurations V_{a1} and ΔV_{a23} are equal to 1200 V, whilst ΔV_{a12} and, thus, V_{a2} and V_{a3} are varied. The results of Scheme C suggest that the light gain has a positive linear dependence on ΔV_{a12} up to $\sim$800 V, where the light gain plateaus to a value of 343.0 ± 4.7 ADU. The gradient of this linear region is 0.45 ± 0.04 ADU/V ($3.75 \pm 0.04 \times 10^{-2}$ ADU/(V/cm)) when fitting a first order polynomial to the first four points of the scheme.
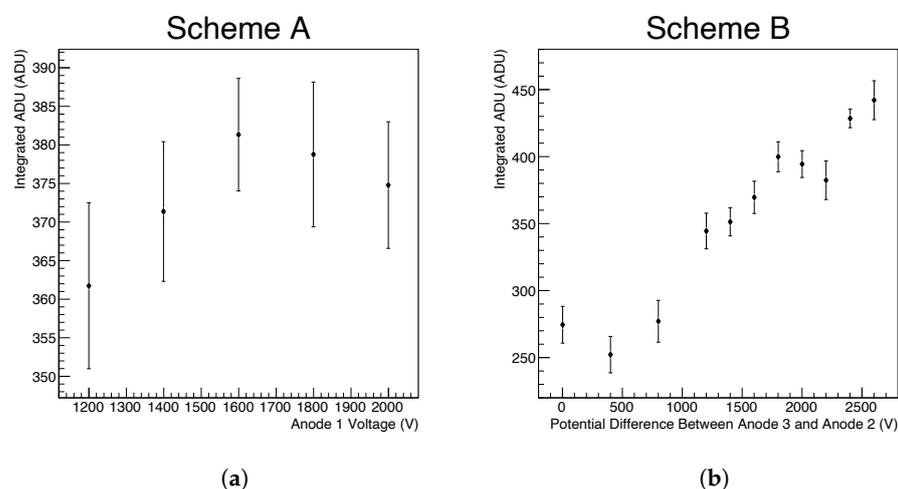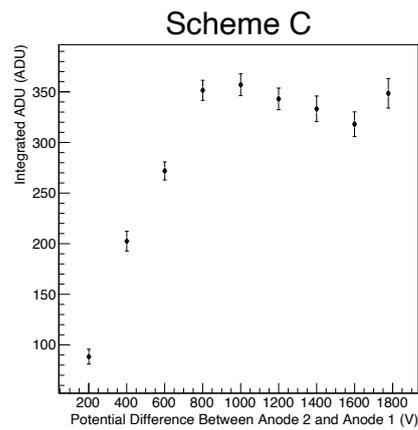

(a)

(b)

Figure 15. *Cont.*

(c)

Figure 15. Light gain measurements of integrated ADU from ^{241}Am source (**a**) vs. anode 1 voltage where the voltage difference between anode 1 and 2 (anode 2 and 3) is kept constant at $\Delta V_{a12} = \Delta V_{a23} = 1200\,\text{V}$, (**b**) vs. voltage potential difference between anode 2 and anode 3 whilst the voltage difference between anodes 1 and 2 is maintained at 1200 V, and (**c**) vs. potential difference between anodes 1 and 2 whilst the potential difference between anode 2 and 3 is maintained at 1200 V. All of the measurements have been performed in the same fill of pure argon at 3 bar absolute pressure.

We speculate on the origin of the plateau after the $\sim$700 V observed in Scheme C. One hypothesis is that the plateau occurs when the electric field between anodes 1 and 2 (E_{a12}) equals that between anodes 2 and 3 (E_{a23}). When $E_{a12} > E_{a23}$, fewer electrons will be able to move from the gap between anode 1 and anode 2 into the gap between anode 2 and 3 and, thus, there are fewer electrons available for amplification and/or excitation. The analysis of the circuit response and the inferred capacitances (Section 6.3.1) suggest that the distance between anode 1 and 2 is $1.20 \pm 0.05\,\text{mm}$, and the distance between anode 2 and anode 3 is $2.0 \pm 0.2\,\text{mm}$. Using these distances, we obtain $E_{a12} = 5.83 \pm 0.87\,\text{kV cm}^{-1}$ and $E_{a23} = 6.0 \pm 0.6\,\text{kV cm}^{-1}$. Because both value agree with each other, we find $E_{a12} = E_{a23}$, where the plateau occurs. The fact that the increase in light gain stops when $E_{a12} = E_{a23}$, thus, could be related to a change in electron transparency of anode 2. However, observing a plateau and not a simple drop in the light gain's gradient with increasing voltage is surprising, because, for a plateau to arise, the hypothesised electron loss needs to be exactly compensated by an increased light yield from the electrons in the anode 1 and 2 gap. During the Scheme B measurements, E_{a12} was held at a value of $10.00 \pm 4.16\,\text{kV cm}^{-1}$, using the distances that were discussed before. E_{a23} was scanned from 0 to $13.0 \pm 1.3\,\text{kV cm}^{-1}$. $E_{a23} > E_{a12}$ is fulfilled from a ΔV_{a23} of $2000 \pm 200\,\text{V}$ onwards and a plateau should be visible, as in the case of Scheme C. The data presented in Figure 15b are not sufficient for concluding that the trend reaches a plateau at the stated value, nor is it sufficient for the opposite, as the plateau's expected position is too close to the end of the ΔV_{a23} voltage scan. With the maximal E_{a12} in its error-bars, a ΔV_{a23} of 2800 V would be required to reach the cross over between the rising and plateau region.

The conclusion that is drawn form this study is that the light gain in the amplification region depends most strongly on the potential differences between the meshes, rather than the absolute voltage on the mesh wires.

5.4.3. Number of Photons in Amplification Region per Primary Electron

It is necessary to make use of additional measurements and some assumptions in order to calculate how many photons are produced in the amplification region per primary electron in the drift volume. In this work, we do not attemptto calculate the relationship between primary electrons in the drift volume and the number of electrons in the amplification region directly (by considering diffusion, mesh transit, and charge gain), as we cannot externally constrain all of the variables. Instead, we calculate the number of photons per

second in the amplification region (N_γ) from the ^{241}Am source using the observed ADU in the CCD, as follows:

$$N_\gamma = \frac{\text{ADU}_{\text{obs}}}{(\text{Conversion Gain}) \times QE^*(\varepsilon) \times \Omega \times \left[T_{\text{window}} \times T_{\text{lens}} \times T_{\text{cathode}} \times T_{\text{anode}}^2 \right]},$$

where ADU_{obs} is the observed ADU from the CCD per second in the region around the source. In our measurements, the maximum value reached was $225 \pm 10\,\text{ADU/s}$, *cf.* Figure 15b, divided by the exposure time of 2 s. The conversion gain that is provided by the manufacturer is 1.5 ADU per electron. The quantum efficiency QE^* is a function of the incident photon energy, for light in the near infrared, the manufacturer specifies $60 \pm 10\%$ of photons being converted into electrons. In principle, we could be seeing light in the visible, infrared, and ultraviolet from the argon scintillation. However, since both the quantum efficiency of the CCD and the transmission probability through the quartz windows have a rapid drop off below 350 nm, in this calculation we assume that we are not sensitive to the UV light. Some photons will not make it from the amplification region to the CCD. The geometric acceptance of the system, Ω, was calculated to be $(1.1 \pm 0.11) \times 10^{-4}$. $T_{\text{lens}} = 80 \pm 10\%$ and $T_{\text{window}} = 97^{+3}_{-4}\%$ are the transmission probabilities through the lens and quartz window, respectively. In addition, all of the photons that were imaged from the amplification must pass through at least one cathode and one anode mesh, with the majority of them passing through two anode meshes. The transmission probabilities through the cathode and anode meshes are $T_{\text{cathode}} = 0.97$ and $T_{\text{anode}} = 0.89$, respectively. This results in $N_\gamma = (3.8 \pm 0.7) \times 10^6$ photons per second in the amplification region.

We then make a calculation of the expected primary electrons in the drift volume per second, N_e, based on the measured activity of our ^{241}Am source, as follows:

$$N_e = N_\alpha \times \frac{\langle \varepsilon_\alpha \rangle}{W}$$

where $N_\alpha = 10 \pm 1$ kBq is the activity of our alpha source and $\langle \varepsilon_\alpha \rangle = 4.56\,\text{MeV}$ is the expected energy that is deposited by the alpha particles after exiting the source and the energy required for ionization in argon is $W = 26.4 \pm 0.3\,\text{eV/electron}$. This results in $N_e = (1.7 \pm 0.2) \times 10^9$ electrons per second in the imaged part of the drift volume. Combining these two results, we expect there to be a total of $(2.2 \pm 0.5) \times 10^{-3}$ photons in the NIR in the amplification region per primary electron in the drift volume.

6. Charge Readout Analysis and Performance

In this section, we discuss the raw data obtained from the charge readout and the analysis that turns these raw data into physical quantities. We explain the calibration of the TPC charge readout with radioactive sources and cosmic radiation, and report the charge gain obtained with different high voltage settings.

6.1. Anatomy of a Waveform

Signals from the three anode meshes are decoupled from their respective HV line as described in Section 4.5, fed into a pre-amplifier, and digitized. Figure 16 shows an example of a digitized waveform, as a trace of voltage versus time. We define the quantities V_i and t_i to be the digitized voltage and time, respectively, at the ith time sample.
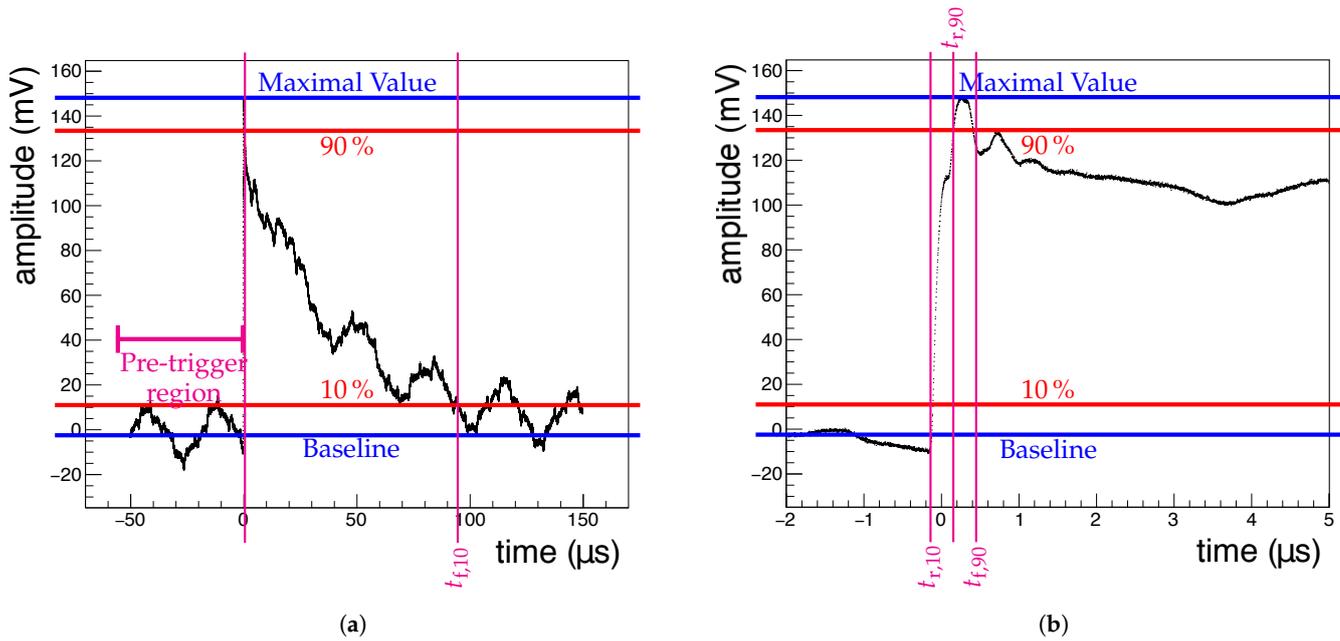
Figure 16. Example for a charge signal, a waveform—(**a**) and (**b**) zoom—with some of its defining features indicated. See the text for more explanations. The first vertical line in (**a**) shows the approximate position of all the vertical lines in the zoomed plot in (**b**).

A waveform is comprised of three characteristic regions in time, as shown on the sample waveform: the period before the digitizer has triggered (*pre-trigger*), the time at which the digitizer triggered, and the period after (*post-trigger*). The pre-trigger region—that is, sample 1 to sample $N_{\text{pre-trig}}$ corresponding to $t = 0$—is used to calculate a mean baseline (*Baseline* in Figure 16) and baseline RMS for a waveform.

The pre-amplifiers are charge-integrating; thus, the maximum voltage of the charge waveform is proportional to the total charge that was collected on an anode. The amplitude (negative amplitude) of a waveform is taken to be the largest (smallest) V_i value of the waveform, $\max(V_{i=0...N})$ ($\min(V_{i=0...N})$), subtracted by the mean baseline. We distinguish the properties of negative polarity pulses from positive ones by adding a "negative" to the respective property's name where appropriate.

The start-time ($t_{r,10}$ shown in Figure 16b) of a pulse is found by looking backwards in time (examining the samples with decreasing sample number i) from the sample with the maximum (minimum) V_i value to the point in time where the waveform reaches 10% of its amplitude value. The point at which the waveform reaches 90% ($t_{r,90}$ in Figure 16b) of its amplitude is identified in the same manner. From the maximum voltage, the waveform decays exponentially with a time-constant, depending on the pre-amplifier chip used. Likewise, the $t_{f,10}$ and $t_{f,90}$ points on the tail of the waveform are found by finding the point after the maximum (minimum), where the amplitude first falls below 90% and 10% of the peak value. A pulse's rise time (fall-time) is calculated as the difference between $t_{r,10}$ and $t_{r,90}$ ($t_{f,90}$ and $t_{f,10}$).

In addition to the above, the RMS of a charge waveform is calculated as:

$$WaveformRMS = \sqrt{\frac{1}{N} \sum_{i=1}^{j} V_i^2} \qquad (6)$$

where j is the number of the last sample. The *BaselineRMS* is calculated in a similar manner, but only taking V_i in the pre-trigger region into account.

6.2. Waveform Cleaning

In order to obtain the most accurate values of the parameters described above, we apply a series of cleaning steps to the waveforms before calculating the parameters. Cuts are made to select waveforms based on their Baseline and BaselineRMS. The mean of the Baseline values of all waveforms in a run is calculated. The waveform is rejected if the baseline mean of a waveform is not within a 5 RMS interval of the mean of all Baseline values. Similarly, if the BaselineRMS of waveform is not within a 5 RMS interval of the mean of all BaselineRMS values, the waveform is cut. This cut allows for removing all waveforms with anomalous fluctuations of the baseline, as occurring e.g., during sparks. Figure 17 shows a spectrum of the anode 1 Baseline values before and after applying these cuts.
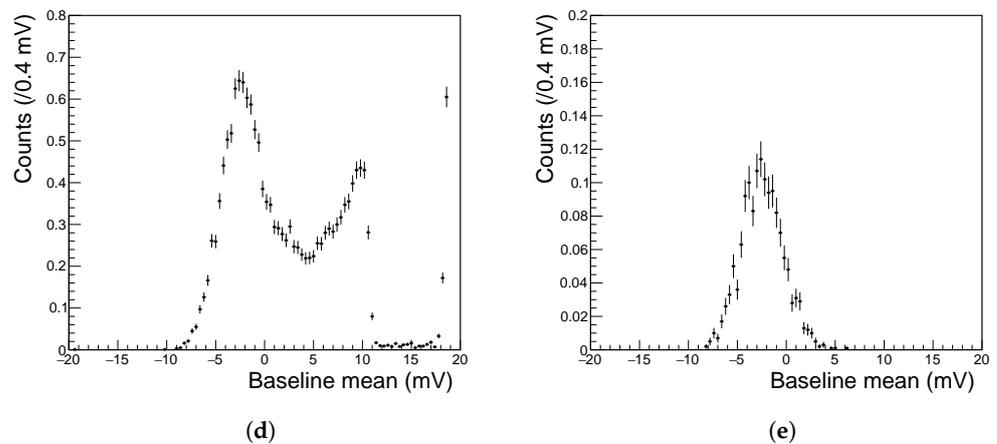

(d) **(e)**

Figure 17. Anode 1 Baseline spectrum (**a**) before cleaning, and (**b**) after cleaning. Waveforms with large Baseline values are cut, which removes spark events.

Waveforms with a Baseline above the trigger threshold are cut. Furthermore, a set of simultaneously recorded waveforms is rejected when the maximum V_i value of the anode 3 waveform is below the trigger threshold. This is because we trigger the simultaneous readout of all three anodes with the anode 3 signal. The corresponding anode 1 and 2 waveforms can still be used in an amplitude measurement in cases where only the anode 3 waveform's maximal V_i is above its trigger threshold.

Checks are made to identify the events containing sparks and such events with a damaged pre-amplifier. An "event" contains all of the waveforms recorded during the exposure time of the simultaneously taken CCD frames. In the case of sparks, the pre-amplifiers' baselines moves substantially, and it takes time for the pre-amplifier to return to the pre-spark status. Thus, an event is flagged as spark event when it contains more than five waveforms with a Baseline above the trigger threshold. When a pre-amplifier gets damaged, the result is a flat waveform. Hence, we flag events where the maximum value is very close to the baseline ($\max(V_i) < Baseline \times 1.02$) and ($\max(V_i) > Baseline \times 0.98$) as having been taken with a damaged preamp.

Finally, waveforms are accepted or rejected based on their rise time and *Peak Time*. The Peak Time is the time value t_j in a waveform for which $V_j = \max(V_i)$, $i \in 0 \dots N$. We calculate the rise time as the time difference between: $t_{r,90}$ and $t_{r,10}$. For anodes 2 and 3, waveforms with a rise time above 5 μs or a Peak Time, which is not within a 5 μs interval around $t = 0$ are cut. For anode 1, the peaks are not always visible above the noise. Waveforms with a long rise time or a Peak Time outside of $t < \pm 5$ μs are rejected for the anode 1 amplitude measurement, but the corresponding waveforms shown in anode 2 and 3 are not cut. These time values are conservative cuts, being chosen far above the pre-amplifiers specified rise time of 3 ns, which help to remove waveforms that have been

triggered by noise. Tables 2 and 3 show the fraction of the analyzed waveforms that are rejected by each data cleaning cut.

Table 2. The fraction of analyzed waveforms rejected for each data cleaning cut for a run where no sparking was observed.

Cut	Surviving Signals	
	Single Cut	**Cuts Applied Subsequently**
No Cuts	100 %	100 %
Baseline < Trigger-threshold	99.97 %	99.97 %
Baseline within mean interval	99.97 %	99.97 %
BaselineRMS within interval	99.99 %	99.97 %
$\max(V_i)$ > Trigger threshold	11.25 %	11.23 %
rise time < 5 µs	61.23 %	9.59 %
Peak Time < 5 µs	20.56 %	9.59 %

Table 3. Fraction of analyzed waveforms rejected for each data cleaning cut for a run containing spark events.

Cut	Surviving Signals	
	Single Cut	**Cuts Applied Subsequently**
No Cuts	100 %	100 %
Baseline < Trigger-threshold	53.26 %	53.26 %
Baseline within mean interval	26.85 %	26.85 %
BaselineRMS within interval	68.29 %	26.85 %
$\max(V_i)$ > Trigger threshold	5.64 %	5.22 %
rise time < 5 µs	51.53 %	4.35 %
Peak Time < 5 µs	14.92 %	4.25 %

6.3. Gas Gain Measurement

In this section, the charge gain of the three anode amplification stage is calculated from the amplitude spectra that are discussed above. Features in the spectra have to be related to a known energy deposition inside the HPTPC. A known energy deposit can be realized using a radioactive source e.g., ^{241}Am (*cf.* beginning of Section 5). Primary ionization electrons (Q_e) from converted γ-rays or α particles drift towards the anode meshes and are amplified there. The amplification factor, the charge gain of the amplification region G_amp, depends on the meshes' configuration, such as inter mesh distance and HV settings. After charge signals are decoupled from the HV line, they are amplified by the pre-amplifiers (G_preamp). Thus, the amplitude A of a waveform relates to Q_e, as

$$A[\mathrm{mV}] = f \cdot G_\mathrm{preamp}\left[\mathrm{mV\,pC}^{-1}\right] \cdot G_\mathrm{amp} \cdot Q_\mathrm{e}[\mathrm{pC}] \quad . \tag{7}$$

The factor f is another dimensionless factor that we introduce to describe the (attenuating) effects of the readout circuit on the signal height. G_preamp and f are determined with dedicated measurements to calibrate the readout circuit.

6.3.1. Pre-Amplifier and Circuit Calibration

Cremat CR-112 and CR-113 charge sensitive pre-amplifiers, hosted on a CR-150-R5 evaluation board, are the pre-amplifier chips employed. The gain of the pre-amplifier chips is calibrated by injecting pulses into the evaluation board test input (1 pF input capacitance). We chose rectangular pulses with a pulse height V_input, and a low frequency and long width when compared to the pre-amplifiers decay time of a few 100 µs. These pulses are recorded with the HPTPC's data acquisition system and then analysed with the analysis chain described above, but without applying cleaning cuts since no noise signals are present when not applying HV to the detector. For a given test pulse height, the resulting

amplitude spectrum features one peak. The ratio of the peak's mean amplitude to the input pulse height gives G_{preamp} when taking the input capacitance of pre-amplifiers into account. When testing several chips, the average gain of the CR-112 chips is measured to be $G_{\text{preamp}}^{\text{CR}-112} = 11.7 \pm 0.6\,\text{mV pC}^{-1}$, and the average gain of the CR-113 chips was measured to be $G_{\text{preamp}}^{\text{CR}-113} = 1.24 \pm 0.06\,\text{mV pC}^{-1}$. These values are consistent with the values that are provided by the supplier of $13\,\text{mV pC}^{-1}$ and $1.3\,\text{mV pC}^{-1}$, respectively.

A detailed description of the HPTPC's circuit response to test pulses can be found in [29]. To perform these tests, one of the three pre-amplifiers is disconnected from its bias box ($S_{\text{anode}i}$ in Figure 7), and test pulses are injected where it is usually connected. Doing so induces signals on the other two anode meshes, which are read out. Table 4 shows the inter-mesh capacitances that were measured with a digital multimeter as well as the results from a fit to the data obtained during the test-pulse campaign.

Table 4. Mesh capacitances determined by a fit [29] and by a direct measurement with a multimeter.

Measurement Taken	Capacitance's between Anode 1/2 [nF]	χ^2/N_{dof} of Anode 1/2	Capacitances between Anode 2/3 [nF]	χ^2/N_{dof} of Anode 2/3	Capacitances between Anode 1/3 [nF]
fit	7.3 ± 0.3	0.76	4.4 ± 0.4	0.35	-
Multimeter reading	6.06 ± 0.05	-	3.72 ± 0.05	-	2.16 ± 0.05

The capacitance that is determined by measuring pulse amplitudes and multimeter measurement differs by 17%. This difference is likely due to the fact that the multimeter measurement is performed close to the detector, i.e., no long cables and other parasitic capacitances are present. The distance between the mesh planes can be determined while knowing the capacitances:

$$C = \epsilon_o \frac{A}{d},\tag{8}$$

where C is the capacitance, ϵ_0 the vacuum permittivity, A the area of the mesh planes, and d is the distance between two mesh planes. This assumes that the meshes can be approximated as a parallel plate capacitor. Inserting our mesh geometry into the calculations presented in [30] shows that such an approximation overestimates (underestimates, respectively) the actual capacitance (mesh distance, respectively) by less than 10%. Furthermore, we use $\epsilon_{\text{Ar}} = 1$, which is accurate to a level that is better than 1‰ [31], hence $\epsilon_{\text{Ar}}\epsilon_0 = \epsilon_0$. We can calculate that anode 1 and 2 are $1.20 \pm 0.05\,\text{mm}$ apart, and the distance between anode 2 and anode 3 is $2.0 \pm 0.2\,\text{mm}$. These values are likely too small, since the approximation used underestimates the distance, as mentioned before. During construction, we aimed for a spacing of $0.5\,\text{mm}$ ($1\,\text{mm}$) between anode 1 and 2 (anode 2 and 3) (*cf.* Section 4.3). The values determined here have the right order of magnitude and are close to the design values. The difference can be due to the fact that the exact thickness of the glue layers in the amplification region is not known; therefore, the design values are most likely a lower limit.

Figure 18 shows an example where a test pulse is coupled into S_{anode1} at the anode 1 bias box, while the anode 2 and anode 3 signals are amplified and digitized. In the figure, anode 2 signal is saturated, whilst the decay of the anode 3 signal shows a change of decay constant around $\sim 20\,\mu\text{s}$. A systematic study of the amplified signals' peak height ($V_{\text{output}}^{\text{amp}}$) revealed that, as soon as one pre-amplifier is saturated, the signal on the other pre-amplifier shows a modified decay that is similar to what is visible in Figure 18 [29]. This behavior affects the measured amplitude, as shown in Figure 19: The points for anode 2 feature two distinct regions: An initial region of linear increases up until an output voltage of $3330 \pm 20\,\text{mV}$, where the pre-amplifier saturates and the region after that.
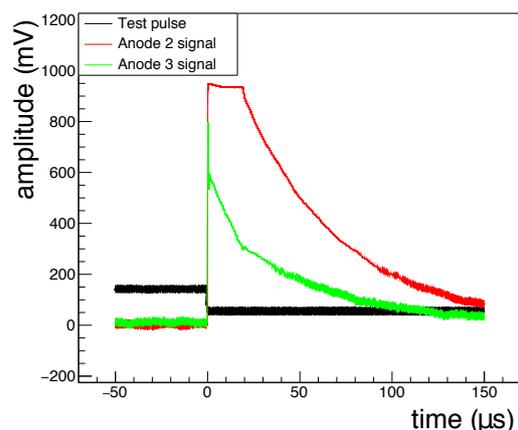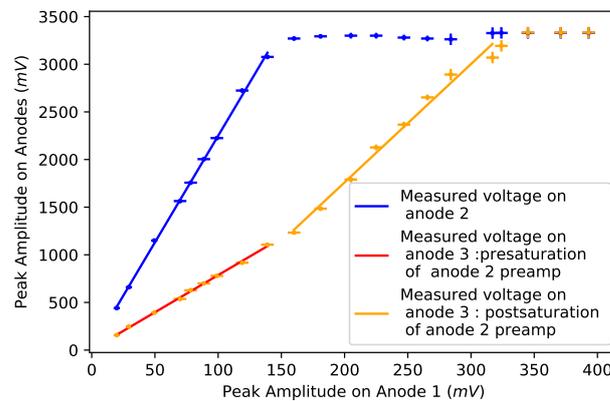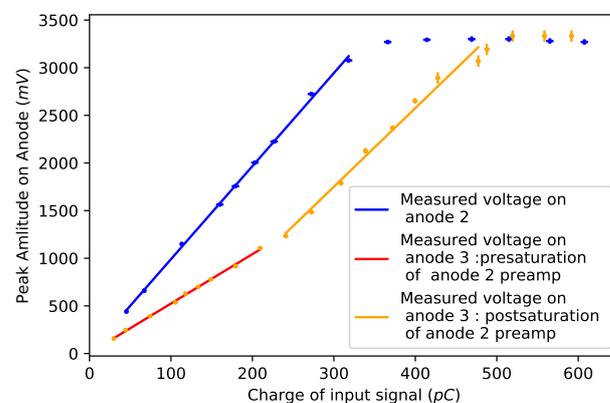
Figure 18. Waveform of a test pulse, coupled into the anode 1 mesh and the resulting amplified pulses (CR-112), as digitized by the HPTPC's data acquisition system.

The saturation value is in line with the manufacturer's technical specification for the output swing of ± 3 V. Figure 19b shows the same data as Figure 19a, but as function of the charge that arrives at the input of the respective pre-amplifier. The charge is calculated using V_{input} and the circuit elements that are shown in Figure 7. The slope of the anode 2 data before saturation in the plot gives the pre-amplifier gain ($G_{\text{preamp}}^{\text{CR}-112} = 11.7 \pm 0.6 \, \text{mV} \, \text{pC}^{-1}$) that is multiplied by f^{a2}, which describes signal attenuation and losses in the circuit (*cf.* Equation (7)). The fitting of a polynomial of order one to the data points, corresponding to the anode 2 line in Figure 19a, yields $f^{a2} \cdot G_{\text{preamp}}^{\text{CR}-112} = 9.8 \pm 0.1 \, \text{mV} \, \text{pC}^{-1}$; Table 5 shows the corresponding value for f^{a2}.

However, for anode 3, three regions can be identified in Figure 19a. There are two regions of distinct linear increase, but with different gradients. The first region—up to a V_{input} of 150 mV—ends at the point when the anode 2 pre-amplifier saturates. From this point onwards, two decay constants are observed in anode 3 waveforms, similar to what is shown in Figure 18. In the second region, the increase is still linear, but with a different slope than in the first region and the third region covers the saturation of the anode 3 pre-amplifier. When the anode 2 pre-amplifier saturates, the AC signal current can no longer simply flow through its input and feedback capacitor, and the signal sharing is modified. This feedback is then seen in the detector as more charge being measured by the anode 3 pre-amplifier than expected. It has been confirmed that this behavior is indeed due to the anode 2 pre-amplifier saturating. Removing this pre-amplifier from the circuit results in anode 3 signals with only one decay constant and no change in gradient— similar to what is shown for anode 2 in Figure 19a. A fit of a polynomial of order one yields $f^{a3} \cdot G_{\text{preamp}}^{\text{CR}-112} = 5.18 \pm 0.07 \, \text{mV} \, \text{pC}^{-1}$ for anode 3 before the anode 2 saturation and $f_{\text{post}}^{a3} \cdot G_{\text{preamp}}^{\text{CR}-112} = 8.3 \pm 0.4 \, \text{mV} \, \text{pC}^{-1}$ after the saturation. Table 5 shows the circuit response f that is obtained by comparing the measurements of $f \cdot G_{\text{preamp}}$ to the bare $G_{\text{preamp}}^{\text{CR}-112}$ measurements at the beginning of this section.

(**a**)

(**b**)

Figure 19. Peak height ($V_{\text{output}}^{\text{amp}}$) measured by the anode 2 and anode 3 readout channel (with pre-amplifier) for test pulses injected into the amplification region via the anode 1 mesh. Both plots show the same data with different units on the horizontal axis: (**a**) $V_{\text{output}}^{\text{amp}}$ as function of input test pules signal height (V_{input}) and (**b**) as a function of the charge seen at the pre-amplifier input. One polynomial of order ($P1$) one is fitted to the anode 2 (blue) measurement and two separate $P1$s are fitted to the different regions on anode 3. One in the pre-saturation region of the anode 2 pre-amplifier (red) and one in the post-saturation region of anode 2 pre-amplifier (orange).

Table 5. Using the measured pre-amplifier without the circuit response ($G_{\text{preamp}}^{\text{CR}-112} = 11.7 \pm 0.6$ mV pC^{-1}) and the measurements of the pre-amplifiers connected to the detector $f \cdot G_{\text{preamp}}$, the circuit response modification-factor f is determined [29].

Anode	$f \cdot G_{\text{preamp}}$ [mV/pC]	Modification Factor f
anode 2	9.8 ± 0.1	0.754 ± 0.007
anode 3 Pre-saturation	5.18 ± 0.07	0.398 ± 0.005
anode 3 Post-saturation	8.3 ± 0.4	0.64 ± 0.03

Finding $f = 1$ would imply that there are no signal losses or attenuation effects in the circuit. The f values that are measured here show a substantial attenuation that can be corrected for since f is constant as a function of amplitude. These losses may occur through the resistive elements that are shown in Figure 7. The change in f on anode 3 when the anode 2 pre-amplifier is saturated makes this correction slightly more complicated. The capacitances of the amplification region and the available pulse generator did not allow for driving the anode 3 pre-amplifier into saturation to examine whether a similar feed-back occurs on anode 2. In general, events with either pre-amplifier being saturated only occur

rarely, as do events where the signal amplitude on anode 2 is higher than on anode 3 due to the way that the amplification region is biased.

6.3.2. Charge Gain of the Amplification Region

This section discusses the analysis of charge waveform data taken simultaneously with the CCD frames used for the light analysis described in Section 5.4. All of the data were taken in the same TPC fill of pure argon at 3 bar absolute pressure. The three voltage schemes—A, B, and C—are described in detail in the previous section.

Determining the Am-241 Alpha Decay Peak Amplitude

After data cleaning (Section 6.2) and taking the calibration that is discussed in Section 6.3.1 into account, we create amplitude spectra for each anode per voltage setting, as shown in Figure 20. The number of entries in the amplitude spectra for each voltage configuration varies between 100 and 2500, with an average of 910 entries per configuration. This variation is caused by the fact that, at higher voltage settings, a greater number of waveforms are recorded and survive the cleaning cuts. From the results that are presented in Section 5.4 (and Section 5.3), we are confident that we should see the α particles from the ^{241}Am decay in the waveform amplitude spectra. Whilst the qualitative example spectrum in Figure 8 does not account for the gas gain and the electronic noise, the measured amplitude spectra should show some resemblance to this simulation. The measured amplitude spectra (Figure 20) appear as an exponentially falling background with a clear peak. This peak corresponds to the deposit of the $\sim$4.5 MeV α particles from the ^{241}Am decay. The exponential background is a mix of the expected cosmic radiation background, of the ^{241}Am X-ray signals and noise triggers. The amplitude spectra are fitted with the function

$$s(\text{amplitude}) = \exp\left\{p_0 + p_1 \cdot \text{amplitude}\right\} + p_2 \cdot \exp\left\{-0.5 \cdot \left(\frac{\text{amplitude} - p_3}{p_4}\right)^2\right\}$$
$$+ p_5 \cdot \exp\left\{-0.5 \cdot \left(\frac{\text{amplitude} - p_6}{p_7}\right)^2\right\}, \tag{9}$$

where the first term is an exponential function to fit the noise, and X-ray and γ-ray background, and the second term is a Gaussian function to fit the α-peak. The third term is a second Gaussian function that fits the higher amplitude entries of the spectra, where the spectra are shaped by cosmic muons. Figure 20 shows examples of these fits.
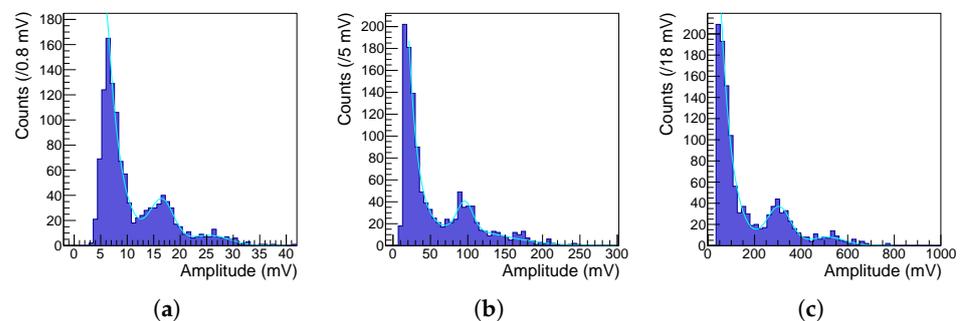

| (a) | (b) | (c) |

Figure 20. The waveform amplitude spectra for anodes (**a**) 1, (**b**) 2, and (**c**) 3. The counts shown on the vertical axis are normalized to the time of one CCD exposure, i.e., 2 s. The spectra are fitted with an exponential plus two Gaussian functions. The amplitude spectra shown are summed data over 15 consecutive runs taken at the same voltage settings, $V_{a1} = 1200$ V, $V_{a2} = 2400$ V, $V_{a3} = 3600$ V, and $V_c = -6000$ V.

The mean of the Gaussian fitting the α-peak from the ^{241}Am decay, p_3, is extracted and taken as a measure for the mean energy deposit of the α particles. In Figure 21, the

α-peak position is plotted against the varied voltage in the respective voltage scheme. The peak position uncertainties shown in the plots are the fit uncertainties on the mean of the Gaussian, scaled by the χ^2/N_{dof} of the fit, for fits where $\chi^2/N_{\text{dof}} > 1$.
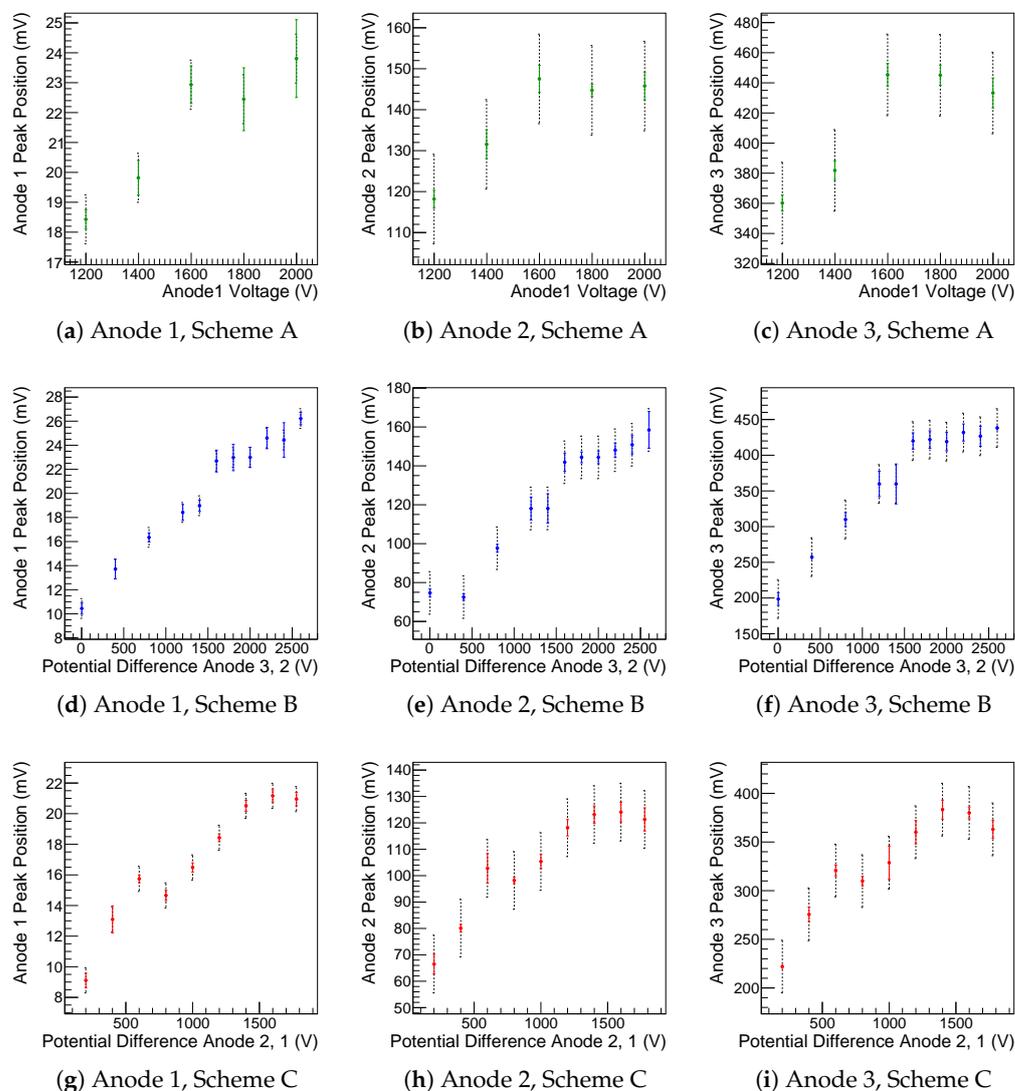

Figure 21. Plots of the position of the α-peak in the respective amplitude spectra. In the first row (**a**–**c**) the peak position is plotted vs. anode 1 voltage (Scheme A). During Scheme A, the voltages of all three anodes are increased in steps of 200 V, while the potential difference between anodes is kept constant. In the second row (Scheme B: **d**–**f**) the peak position is plotted vs. the potential difference between anodes 2 and 3 (ΔV_{a23}). During the measurement V_{a1}, V_{a2} and ΔV_{a12} are kept constant. Third row (Scheme C: **g**–**i**): Peak position vs. the potential difference between anodes 1 and 2 (V_{a12}), while V_{a1} and ΔV_{a23} are kept constant. All of the measurements have been made in the same gas fill of 3 bar absolute of pure argon.

For Scheme A, the peak position is plotted against the voltage of anode 1 (Figure 21, first row), for Scheme B the peak position is plotted against the potential difference between anodes 2 and 3 (Figure 21, second row), and for Scheme C the peak position is plotted against the potential difference between anodes 1 and 2 (Figure 21, third row).

Gas Gain as a Function of Voltage for the Three Voltage Schemes

Gas quality degradation needs to be considered before calculating the gas gain for the three voltage schemes A, B, and C from the values in the amplitude spectra. Degrading gas quality can have a significant effect on the gain measurements, and so we took data at

identical gas, pressure, and bias voltage settings every 24 h to obtain calibration correction, as the data used in this analysis were taken over three days.

We reconstruct the peak position in the amplitude spectra of these calibration runs. After, the gas quality calibration is fit to these data points vs. the measurement time. The correction function is $y(\text{time}) = m \cdot \text{time} + b$, where the values of (m, b) are $(0.8 \pm 0.2\,\text{mV/day}, -1 \pm 5\,\text{mV})$, $(11 \pm 2\,\text{mV/day}, -135 \pm 42\,\text{mV})$ and $(27 \pm 7\,\text{mV/day}, -277 \pm 141\,\text{mV})$ for anode 1, anode 2, and anode 3 spectra, respectively, and the calibration is normalized, such that the non-calibrated data and the calibrated data have the same value at the beginning of Scheme C. We observe a drift in the peak position, as can be seen from the slope values of the (m, b) pairs; however, the drift is such that no change could been observed when individually examining the amplitude spectra for each run in a voltage setting.

A systematic uncertainty contribution is assessed to account for this effect, which is represented by the dotted error bars shown in Figure 21. This contribution takes the expected peak position shift over the measurement time in each voltage scheme into account, and it is calculated as the standard deviation of the measured peak positions with respect to the peak position after correction.

Equation (7) now allows for calculating the gas amplification factor of the amplification region, G_{amp}, using

$$G_{\text{amp}} = \frac{A}{f \cdot G_{\text{preamp}} \cdot Q_{\text{e}}} \quad \text{where} \tag{10}$$

$$Q_{\text{e}} = \frac{\langle \varepsilon_\alpha \rangle}{W} \cdot 1.6022 \times 10^{-19}\,\text{C} \quad . \tag{11}$$

We calculate G_{amp} for the amplitude spectra that were measured at each mesh. In the calculation, we use the best-fit peak position of the α-peak in the amplitude spectra to be A, being corrected by the calibration procedure that is described above. Figure 22 shows the gas gain at each anode plotted against the respective voltage in the three voltage schemes.

The goal of this analysis is to determine the dependence of the gain on the absolute voltages of the anodes (V_{a1}, V_{a2}, and V_{a3}) and on the potential differences between the anodes (ΔV_{a12} and ΔV_{a23}). The results of the charge gain measurement for schemes A, B, and C are shown in Figure 22 in the first, second, and third row, respectively, and the gas gains that are measured at the highest and lowest voltage settings for each scheme are presented in Table 6. The voltage range that is covered during the three schemes has been optimized for the light analysis, to the end that: (i) all voltage settings of the three schemes could be taken in one gas fill without significant degradation of the gas fill, (ii) to avoid reaching a voltage regime where sparking occurs, and (iii) to have sufficient overlap between the three voltage schemes. As a result of this, our study of the charge gain of the amplification region only covers a small gain range (Table 6 and Figure 22).

For all three voltage schemes, the measured gas gain increases from anode 1, to anode 2, to anode 3, as is expected from a cascade of amplification stages. The gas amplification factor shown in Scheme C is the lowest overall. Examining the multiplication factor between different meshes, we find $G_{\text{amp}}^{\text{mesh2}} \sim 8 \cdot G_{\text{amp}}^{\text{mesh1}}$ ($G_{\text{amp}}^{\text{mesh2}} \sim 6.5 \cdot G_{\text{amp}}^{\text{mesh1}}$) and $G_{\text{amp}}^{\text{mesh3}} \sim 5.5 \cdot G_{\text{amp}}^{\text{mesh2}}$ ($G_{\text{amp}}^{\text{mesh3}} \sim 6 \cdot G_{\text{amp}}^{\text{mesh2}}$) in scheme A and Scheme B (Scheme C). The highest contribution to the combined gas gain $G_{\text{amp}}^{\text{mesh1}} \cdot G_{\text{amp}}^{\text{mesh2}} \cdot G_{\text{amp}}^{\text{mesh3}}$ is, thus, the contribution of the anode 1 mesh. The dependence of the gain on the various voltages shows a similar functional shape as the light gain reported in Section 5.4.2, Figure 15. Because of the relatively large uncertainties, the results presented in Scheme A are consistent with either a slight dependence or no dependence of the gain on the absolute voltages of the anodes, while ΔV_{a12} and ΔV_{a23} are fixed at 1200 V and are, therefore, consistent with the conclusions of the light gain analysis. The results of schemes B and C are consistent with a positive correlation of gain on ΔV_{a23} and ΔV_{a12}; this is again consistent with the conclusions that are drawn from the light gain analysis. The results of the charge gain

analysis support the conclusions of the light gain analysis, that the electric field between the anodes primarily drives the amplification.
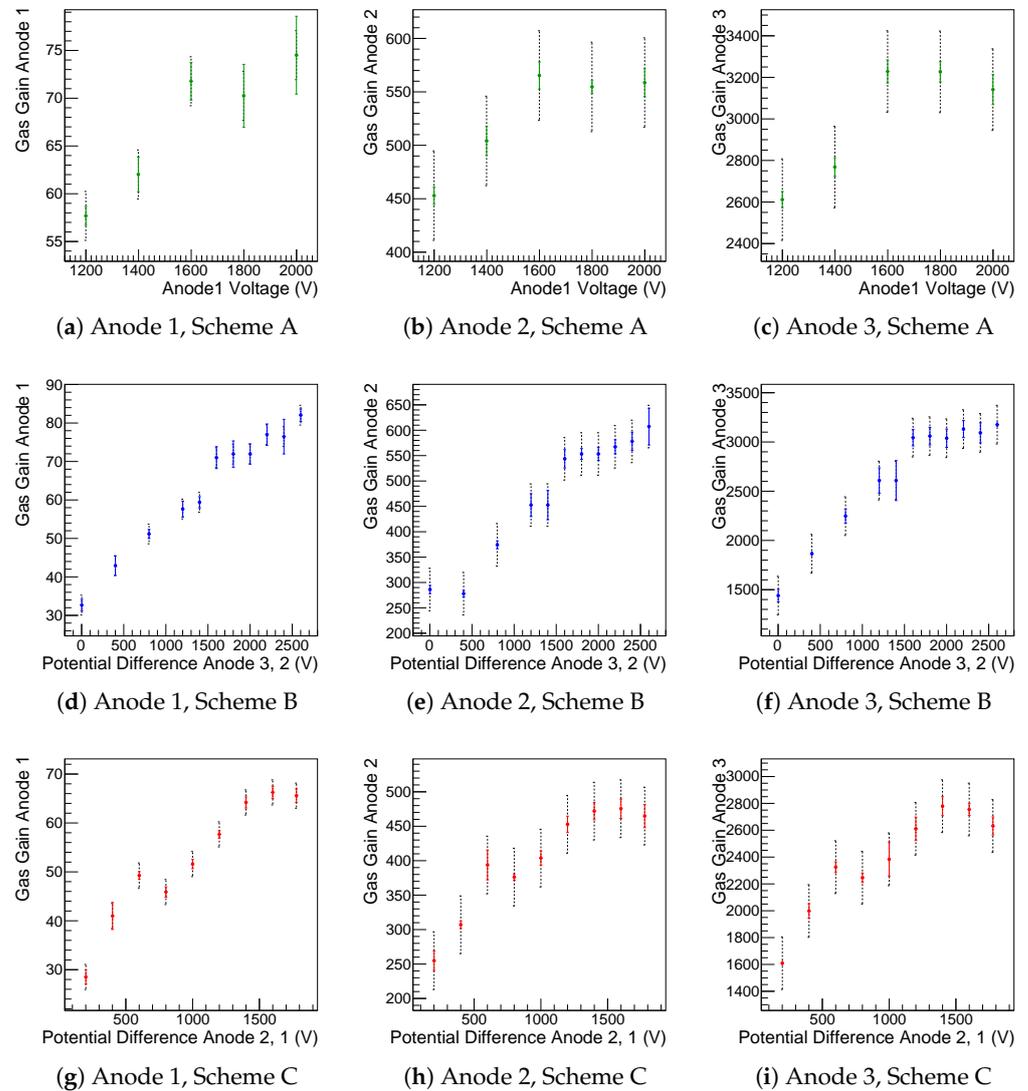

Figure 22. Plots of the calculated gas gain vs. either anode voltage or inter-anode voltage difference. The gain is calculated from the data shown in the respective plot in Figure 21. First row (**a**–**c**): Scheme A, gain vs. anode 1 voltage (V_{a1}), V_{a1}, V_{a2}, and V_{a3} are increased by the same amount, whilst $\Delta V_{a12} = \Delta V_{a23} = 1200$ V. Second row (**d**–**f**): Scheme B, gain vs. the voltage difference between anode 2 and 3 (ΔV_{a23}), V_{a3}, and ΔV_{a23} are increased, whilst $V_{a1} = 1200$ V and $V_{a2} = 2400$ V. Third row (**g**–**i**): Scheme C, gain vs. the anode 1 to anode 2 voltage differences (ΔV_{a12}), V_{a2}, ΔV_{a12}, and V_{a3} are increased whilst keeping V_{a1} and ΔV_{a23} constant. All of the data have been taken in the same gas fill of 3 bar absolute of pure argon.

Table 6. The charge gain measured at the highest at lowest voltage settings of each voltage scheme.

Scheme	Voltage Setting (A1 / A2 / A3) [V]		Gas Gain at Anode 3 at Voltage Setting	
	Lowest	Highest	at Lowest Setting	at Highest Setting
A	1200 / 2400 / 3600	2000 / 3200 / 4400	$(2.61 \pm 0.20) \times 10^3$	$(3.14 \pm 0.20) \times 10^3$
B	1200 / 2400 / 2400	1200 / 3400 / 5000	$(1.44 \pm 0.20) \times 10^3$	$(3.18 \pm 0.20) \times 10^3$
C	1200 / 1400 / 2600	1200 / 3000 / 4200	$(1.61 \pm 0.20) \times 10^3$	$(2.63 \pm 0.20) \times 10^3$

7. Combined Optical and Charge Readout Analysis

In this section, we present the results of the combined optical and charge gain analysis. The optical and charge gain analyses that are described in Sections 5 and 6 were performed

on data taken simultaneously with both readout systems. We investigate the correlation between the optical gain and charge gain in Figures 15 and 22. Figure 23 shows plots of the optical gain against the charge gain for Schemes A, B, and C. Figure 24 shows the ratio of the charge gain to the measured light intensity in ADU as a function of the relevant voltage in the respective voltage scheme. The larger of the two charge gain error bars (shown as dotted line in Figure 23) has been propagated through to produce the error bars that are seen in Figure 24.
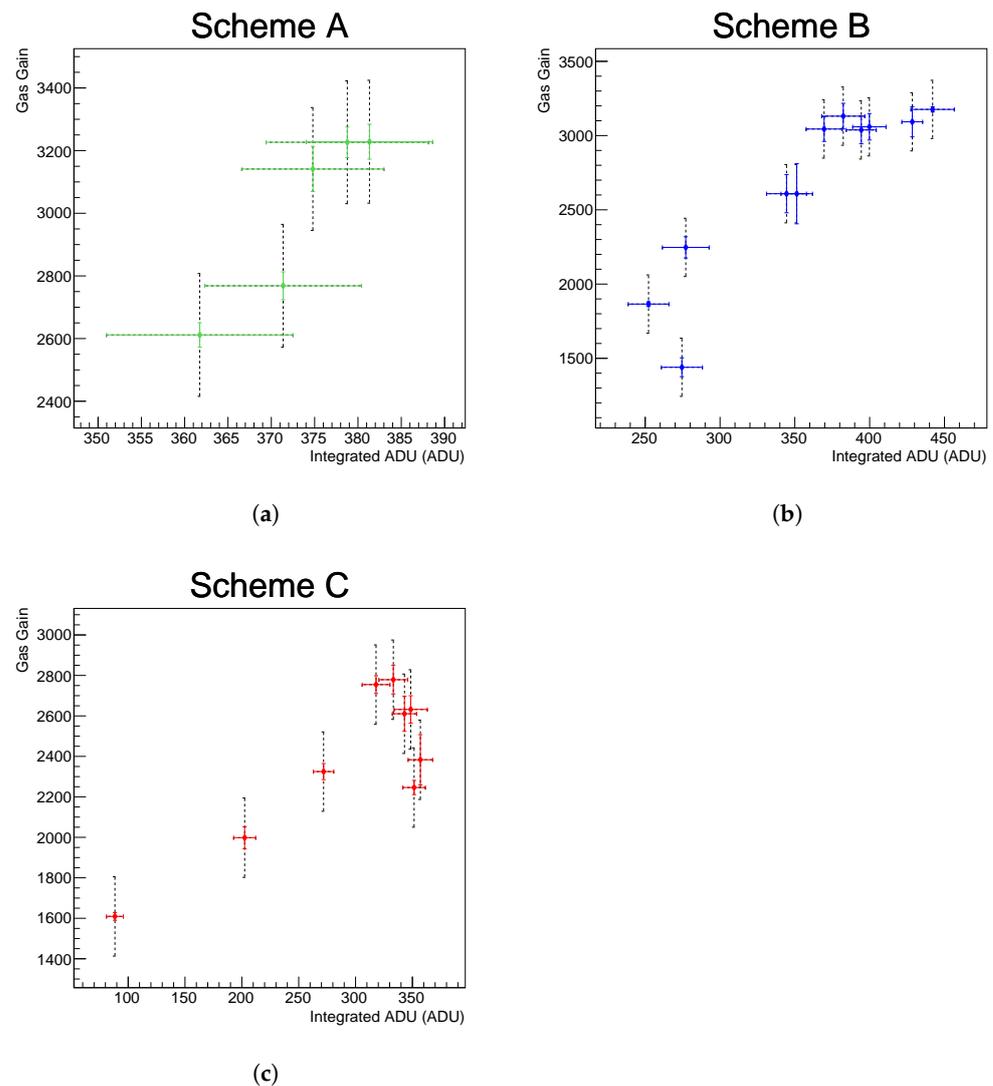

(**a**)

(**b**)

(**c**)

Figure 23. Measured light intensity (Integrated ADU) (Figure 15) plotted against the gas gain measured in the charge readout on anode 3 (Figure 22, right column) for Scheme A (**a**), Scheme B (**b**), and Scheme C (**c**).
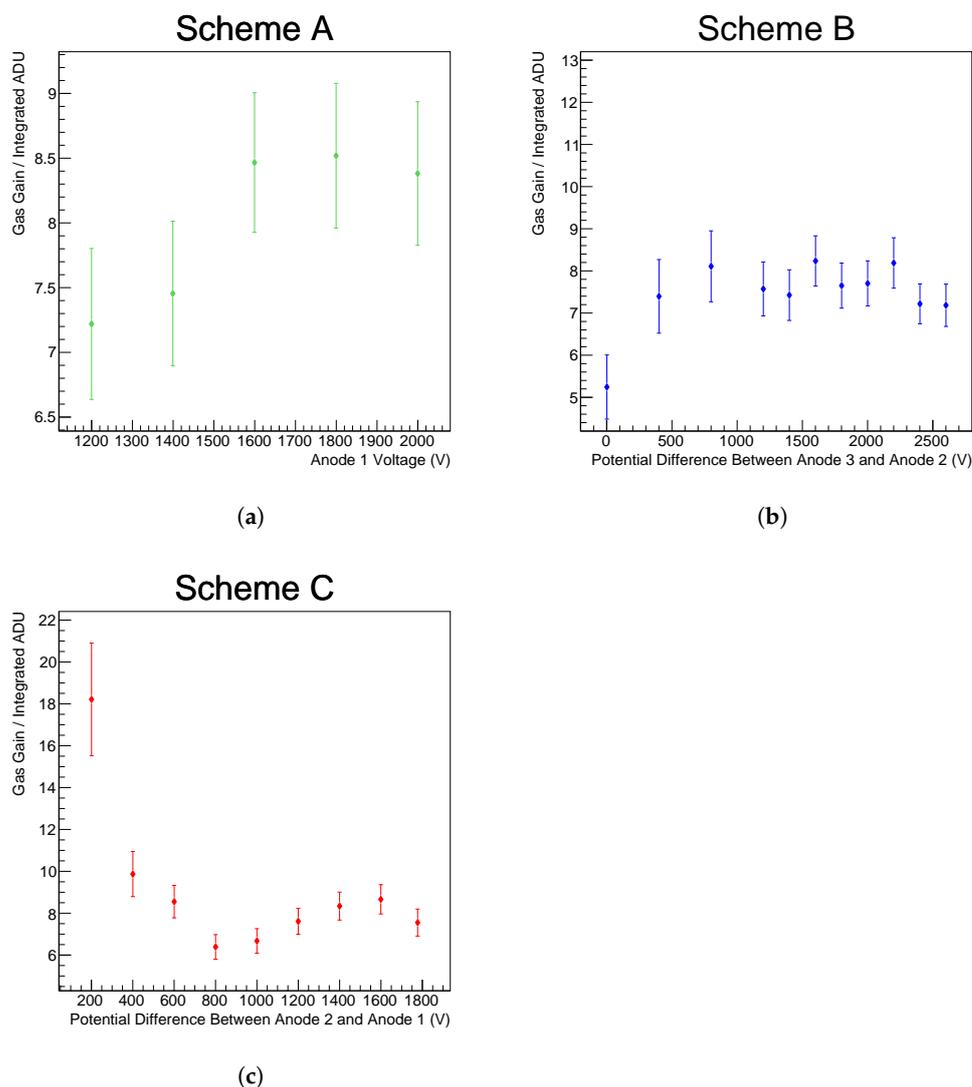
(**a**)　　　　　　　　　　　　　　　　　　　　(**b**)

(**c**)

Figure 24. Ratio of gas gain measured in the amplification region at anode 3 (Figure 22, right column) to the measured intensity (integrated ADU) (Figure 15) vs. (**a**) anode 1 voltage (V_{a1}), where the voltage differences between the meshes is always $\Delta V_{a12} = \Delta V_{a23} = 1200\,\text{V}$ (**b**) potential difference between anode 2 and anode 3 (V_{a23}), while the anode 1 and 2 voltages are kept constant (**c**) potential difference between anodes 1 and 2 (ΔV_{a12}), while V_{a1} is kept constant and ΔV_{a23} is maintained at 1200 V.

We use the Pearson correlation coefficient to measure the correlation factor between the two gain measurements, which takes values between -1 and 1 for fully negative and positive correlated data. The coefficient is zero for uncorrelated data. We take every measured value as the center of a normal distribution and its uncertainty as the distribution's standard deviation in order to take the uncertainties of our measurements into account. From these distributions, 1000 random data series are drawn for each voltage scheme with the same number of points as the original data series shown in Figure 24a–c, and the correlation factor is calculated for each of them. The correlation factors that are quoted in the following are the mean of these 1000 correlation factors and their standard deviation.

In Scheme A, the optical and charge analysis are both found to be consistent with no change in gain. The figures in this section show continued support for this case, as expected. The correlation factor of the data sample that is shown in Figure 23a is 0.50 ± 0.37. Figure 23b,c present a positive correlation between the optical and charge gain in Schemes B and C of 0.85 ± 0.06 and 0.75 ± 0.11. Measuring a correlation between the electron and

photon yield in the amplification region suggests that the measured light is produced within the avalanches and, thus, the light yield increases with the charge gain. In Scheme C, we see a defined saturation of the optical gain above $\Delta V_{a12} = 800\,V$ (as in Figure 15c). This effect is not clearly visible in the charge gain analysis (Figure 22i). However, given the size of the gas gain error bars, it is not possible to confidently exclude this as a possibility.

Figure 24 shows a largely consistent ratio of gas gain to the measured light gain in the integrated ADU of around 8 for all schemes. The only deviation from this ratio occurs at the lowest voltage settings for Schemes B and C. In Section 5.4.3, we found that there are $(2.2 \pm 0.5) \times 10^{-3}$ photons in the amplification region per primary electron in the drift volume when analyzing the voltage setting with the highest light yield. The authors of [20] also examine pure argon at a pressure of 3 bar absolute. For this gas, they measure, albeit with a much smaller detector and a two mesh amplification region with 4 mm distance, a maximal value of ∼0.5 photons per primary electron in the drift volume. This is two orders of magnitude higher than the value that we observe. Furthermore, they observe this photon yield at a charge gain of about 10, while their measured light gain as function of charge gain saturates somewhere in-between charge gains of 5 and 10. In [20], the measurement is performed with an X-ray tube as the radiation source and a photo-diode mounted close to the amplification region. This set-up allows the authors to operate in a low charge gain regime, where the cross-section for excitations can be higher than at larger charge gains where the ionization cross-section dominates.

To improve the concept of an optical HPTPC with a mesh based amplification region, it could be considered to have an amplification stage followed by a region of lower field in which the amplified electrons predominately excite gas atoms or molecules. The difficulty with such a combination of amplification and scintillation regions is that the electron transmissions between two meshes depends on the ratio of the fields on either side—therefore, only a fraction of the electrons from the high-field amplification gap(s) will reach the low-field scintillation gap.

8. Summary

In order to reduce neutrino interaction related systematic uncertainties in future neutrino oscillation experiments, a key measurement is proton-nucleus scattering. Hadronic interactions as particles that are produced in neutrino interactions exit the nucleus and obfuscate the secondary particle multiplicity and kinematics, which causes event migrations between data samples and introduces biases in neutrino event reconstruction. Measurements of protons interacting with nuclei can constrain these hadronic interactions and, thereby, reduce these biases. A HPTPC prototype detector with a three mesh amplification region has been constructed and operated at RHUL and CERN as a first step in the development of a HPTPC that is capable of performing these measurements.

In this work, for the first time, we demonstrate the successful combined optical and charge readout of a hybrid high pressure gaseous TPC with an active volume of ∼0.5 m^3. The optical readout utilizes CCD cameras, which are the most sensitive in the visible part of the wavelength spectrum. Using cameras with an increased range of sensitivity to the VUV or wavelength shifting filters could be beneficial in future research. In a series of pilot measurements, we identified pure argon at an absolute pressure of 3 bar as the gas that is best suited to perform in depth tests of the optical readout performance with a high pressure gas. Our measurements were done using the α particles that were emitted by an Am^{241} source. When using the HPTPC with argon at 3 bar, we were not able to image tracks on an event-by-event basis with the optical readout. This may be due to the large diffusion in pure argon. Integrating over many exposures, we measure an increasing light yield when increasing the electric field between mesh 2 and mesh 3 (E_{a23}), where the mesh number increases for anodes that are further away from drift region. An increase in light yield is also measured when increasing the field between mesh 1 and mesh 2 (E_{a12}). In this case, the light yield reaches a plateau when $E_{a12} \sim E_{a23}$. At the maximum light yield

measured, we find that there are $(2.2 \pm 0.5) \times 10^{-3}$ photons in the amplification region per primary electron in the drift volume.

The analysis of the charge signals reveals that light gain and charge gain are correlated, and that the gas gain at the voltage settings of the maximal light yield is 3000. The first mesh in the cascade contributes the largest fraction of the amplification stages gain of $\sim$70, whilst the following meshes contribute another factor of about 8 and 5.5, respectively.

Author Contributions: Conceptualization, A.B.-F., S.B., D.B., L.C., P.D., J.H., A.K. (Asher Kaboth), J.M., R.N., J.N., R.S., N.S., Y.S. and M.O.W.; Data curation, A.D. (Alexander Deisting), A.V.W., E.A., D.B., Z.C.-W., L.C., A.D. (Adriana Dias), P.D., J.H., P.H.-B., S.J., A.K. (Asher Kaboth), A.K. (Alexander Korzenev), M.M., J.M., R.N., T.N., J.N., W.P., H.R.-Y., S.R., A.T., M.U., S.V., M.W. and M.O.W.; Formal analysis, A.D. (Alexander Deisting), A.V.W., E.A., D.B., Z.C.-W., A.D. (Adriana Dias), P.D., J.H., P.H.-B., S.J., M.M., T.N., W.P., H.R.-Y., A.T. and M.W.; Funding acquisition, G.B., A.B.-F., S.B., A.K. (Asher Kaboth), J.M., R.N., J.N., S.R., R.S. and M.O.W.; Investigation, A.D. (Alexander Deisting), A.V.W., E.A., G.B., A.B.-F., C.B., D.B., Z.C.-W., L.C., A.D. (Adriana Dias), P.D., J.H., P.H.-B., S.J., A.K. (Asher Kaboth), A.K. (Alexander Korzenev), W.M., P.M., M.M., J.M., R.N., T.N., J.N., W.P., H.R.-Y., S.R., R.S., N.S., Y.S., J.S., A.T., M.U., S.V., M.W. and M.O.W.; Methodology, A.D. (Alexander Deisting), A.V.W., G.B., A.B.-F., C.B., S.B., D.B., Z.C.-W., L.C., A.D. (Adriana Dias), P.D., J.H., P.H.-B., S.J., A.K. (Asher Kaboth), A.K. (Alexander Korzenev), W.M., P.M., M.M., J.M., R.N., T.N., J.N., W.P., H.R.-Y., S.R., R.S., N.S., Y.S., J.S., A.T., M.U., S.V., M.W. and M.O.W.; Project administration, A.D. (Alexander Deisting), G.B., S.B., L.C., A.K. (Asher Kaboth), J.M., R.N., J.N. and M.O.W.; Resources, S.B., D.B., L.C., A.K. (Asher Kaboth), J.M., R.N., J.N., S.R. and M.O.W.; Software, A.D. (Alexander Deisting), A.V.W., E.A., P.D., J.H., P.H.-B., S.J., T.N., W.P., H.R.-Y., A.T. and S.V.; Supervision, A.D. (Alexander Deisting), A.V.W., G.B., A.B.-F., S.B., L.C., P.D., A.K. (Asher Kaboth), J.M., R.N., J.N., R.S. and M.O.W.; Validation, A.D. (Alexander Deisting), A.V.W., E.A., D.B., Z.C.-W., L.C., P.D., S.J., A.K. (Asher Kaboth), M.M., J.M., R.N., T.N., H.R.-Y. and A.T.; Visualization, A.D. (Alexander Deisting), A.V.W., E.A., Z.C.-W., A.D. (Adriana Dias), P.D., P.H.-B., W.P. and H.R.-Y.; Writing—original draft, A.D. (Alexander Deisting), A.V.W., Z.C.-W., P.D., A.K. (Asher Kaboth), J.M., W.P., H.R.-Y., A.T. and M.O.W.; Writing—review & editing, A.D. (Alexander Deisting), A.V.W., E.A., D.B., Z.C.-W., L.C., A.D. (Adriana Dias), P.D., P.H.-B., A.K. (Asher Kaboth), J.M., J.N., H.R.-Y. and M.O.W. All authors have read and agreed to the published version of the manuscript.

Funding: This research was funded in part by Science and Technology Facilities Council grant number ST/N003233/.

Institutional Review Board Statement: Not applicable.

Informed Consent Statement: Not applicable.

Data Availability Statement: The raw data of the analysis presented in this paper are not public. Inquires may be send to the corresponding authors.

Acknowledgments: We wish to acknowledge support for summer students from the Ogden Trust and St. Andrews University, and outstanding support during the beam test from Johannes Bernhard of CERN as well as Johan Borg, Rebecca Conybeare, Nicole Cullen, Kate Gould, Maria Khaleeq, Veera Mikola, Duncan Parker, Christopher Thorpe and Simon Williams.

Conflicts of Interest: The authors declare no conflict of interest.

References

1. Abe, K.; Akutsu, R.; Ali, A.; Alt, C.; Andreopoulos, C.; Anthony, L.; Antonova, M.; Aoki, S.; Ariga, A.; Asada, Y.; et al. Constraint on the Matter-Antimatter Symmetry-Violating Phase in Neutrino Oscillations. *Nature* **2020**, *580*, 339–344.
2. Alvarez-Ruso, L.; Sajjad Athar, M.; Barbaro, M.B.; Cherdack, D.; Christy, M.E.; Coloma, P.; Donnelly, T.W.; Dytman, S.; de Gouvêa, A.; Hill, R.J.; et al. NuSTEC White Paper: Status and challenges of neutrino–nucleus scattering. *Prog. Part. Nucl. Phys.* **2018**, *100*, 1–68. [CrossRef]
3. Hayato, Y. NEUT. *Nucl. Phys. Proc. Suppl.* **2002**, *112*, 171–176. [CrossRef]
4. Andreopoulos, C.; Barry, C.; Dytman, S.; Gallagher, H.; Golan, T.; Hatcher, R.; Perdue, G.; Yarba, J. The GENIE Neutrino Monte Carlo Generator: Physics and User Manual. *arXiv* **2015**, arXiv:1510.05494.
5. Hamilton, P.A. A Study of Neutrino Interactions in Argon Gas. Ph.D. Thesis, Imperial College London, London, UK, 2017.
6. MicroBooNE-Collaboration. Measurement of Reconstructed Charged Particle Multiplicities of Neutrino Interactions in Micro-BooNE. *Microboone Public Note* **2017**.

7.   Breskin, A.; Chechik, R.; Fraenkel, Z.; Sauvage, D.; Steiner, V.; Tserruya, I.; Charpak, G.; Dominik, W.; Fabre, J.P; Gaudaen, J.; et al. A Highly Efficient Low Pressure UV Rich Detector With Optical Avalanche Recording. *Nucl. Instrum. Meth.* **1988**, *A273*, 798–804. [CrossRef]

8.   Buckland, K.N.; Lehner, M.J.; Masek, G.E.; Mojaver, M. Low pressure gaseous detector for particle dark matter. *Phys. Rev. Lett.* **1994**, *73*, 1067–1070. [CrossRef] [PubMed]

9.   Fonte, P.; Breskin, A.; Charpak, G.; Dominik, W.; Sauli, F. Beam test of an imaging high-density projection chamber. *Nucl. Instruments Methods Phys. Res. Sect. Accel. Spectrometers, Detect. Assoc. Equip.* **1989**, *283*, 658–664. [CrossRef]

10.   Dujmic, D.; Tomita, H.; Lewandowska, M.; Ahlen, S.; Fisher, P.; Henderson, S.; Kaboth, A.; Kohse, G.; Lanza, R.; Monroe, J.; et al. Observation of the 'head-tail' effect in nuclear recoils of low-energy neutrons. *Nucl. Instrum. Meth.* **2008**, *A584*, 327–333. [CrossRef]

11.   Baracchini, E.; Benussi, L.; Bianco, S.; Capoccia, C.; Caponero, M.; Cavoto, G.; Cortez, A.; Costa, I.; Marco, E.D.; D'Imperio, G.; et al. CYGNO: a gaseous TPC with optical readout for dark matter directional search. *J. Instrum.* **2020**, *15*, C07036–C07036. [CrossRef]

12.   Gai, M.; Ahmed, M.W.; Stave, S.C.; Zimmerman, W. R.; Breskin, A.; Bromberger, B.; Chechik, R.; Dangendorf, V.; Delbar, Th.; France, R.H.; et al. An Optical Readout TPC (O-TPC) for Studies in Nuclear Astrophysics with Gamma-Ray Beams at HIgS. *JINST* **2010**, *5*, P12004. [CrossRef]

13.   Fujiwara, T.; Mitsuya, Y.; Fushie, T.; Murata, K.; Kawamura, A.; Koishikawa, A.; Toyokawa, H.; Takahashi, H. Gas scintillation glass GEM detector for high-resolution X-ray imaging and CT. *Nucl. Instrum. Methods Phys. Res. Sect. Accel. Spectrom. Detect. Assoc. Equip.* **2017**, *850*, 7–11. [CrossRef]

14.   Klyachko, A.; Friesel, D.; Kline, C.; Liechty, J.; Nichiporov, D.; Solberg, K. Dose Imaging Detectors for Radiotherapy Based on Gas Electron Multipliers. *Nucl. Instrum. Methods Phys. Res. Sect. Accel. Spectrom. Detect. Assoc. Equip.* **2011**, *628*, 434–439. [CrossRef] [PubMed]

15.   Brunbauer, F.M.; Lupberger, M.; Oliveri, E.; Resnati, F.; Ropelewski, L.; Streli, C.; Thuiner, P.; van Stenis, M. Radiation imaging with optically read out GEM-based detectors. *JINST* **2018**, *13*, T02006. [CrossRef]

16.   Leyton, M. Directional dark matter detection with the DMTPC m^3 experiment. *J. Phys. Conf. Ser.* **2016**, *718*, 042035. [CrossRef]

17.   Battat, J.; Irastorza, I.; Aleksandrov, A.; Asada, T.; Baracchini, E.; Billard, J.; Bosson, G.; Bourrion, O.; Bouvier, J.; Buonaura, A.; et al. Readout technologies for directional WIMP Dark Matter detection. *Phys. Rep.* **2016**, *662*, 1–46. [CrossRef]

18.   Deaconu, C.; Leyton, M.; Corliss, R.; Druitt, G.; Eggleston, R.; Guerrero, N.; Henderson, S.; Lopez, J.; Monroe, J.; Fisher, P. Measurement of the directional sensitivity of Dark Matter Time Projection Chamber detectors. *Phys. Rev.* **2017**, *D95*, 122002. [CrossRef]

19.   Buzulutskov, A.; Bondar, A.; Grebenuk, A. Infrared scintillation yield in gaseous and liquid argon. *EPLA* **2011**, *52001*. [CrossRef]

20.   Fraga, M.M.R.; Bueno, C.C.; Gonçalves, J.A.C.; Farga, F.A.F.; Ferreira Marques, R.; Policarpo, A.J.P.L. Pressure Dependence of Secondary NIR Scintillation in Ar and Ar-CF$_4$. *IEEE Trans. Nucl. Sci.* **2001**, *48*, 330–335. [CrossRef]

21.   Lindblom, P.; Solin, O. Atomic near-infrared noble gas scintillations I: Optical spectra. *Nucl. Instrum. Methods Phys. Res. Sect. Accel. Spectrom. Detect. Assoc. Equip.* **1988**, *268*, 204–208. [CrossRef]

22.   Fraga, M.M.; Fetal, S.T.G.; Fraga, F.A.F.; Antunes, E.; Gonçalves, J.; Bueno, C.C.; Ferreira Marques, R.; Policarpo, A.J.P.L. Study of Scintillation Light from Microstructure Based Detectors. In Proceedings of the 1999 IEEE Nuclear Science Symposium. Conference Record. 1999 Nuclear Science Symposium and Medical Imaging Conference (Cat. No.99CH37019), Seattle, WA, USA, 24–30 October 1999.

23.   Biagi, S. Magboltz 2. In *CERN Computer Newsletter No.2000-001 in Section 'Scientific Applications and Software Engineering'*; CERN: Geneva, Switzerland, 2000.

24.   Ritchie-Yates, H. Commissioning a New Particle Detector Technology: The High Pressure Time Projection Chamber. Ph.D. Thesis, Royal Holloway University of Londonät Egham (UK), Egham, UK, 2018.

25.   International Atomic Energy Agency. Nuclear Data Section. 2019. Available online: https://www-nds.iaea.org/ (accessed on 10 June 2020).

26.   Henderson, S.W. An Assessment of the Sensitivity of a Low Pressure Time Projection Chamber to the Direction of WIMP-Induced Nuclear Recoils. Ph.D. Thesis, Massachusetts Institute of Technology, Cambridge, MA, USA, 2006.

27.   Smirnov, I. Modeling of ionization produced by fast charged particles in gases. *Nucl. Instruments Methods Phys. Res. Sect. Accel. Spectrometers, Detect. Assoc. Equip.* **2005**, *554*, 474–493. [CrossRef]

28.   Baraka, K.; Folkestad, A.; Frolov, E.; Heijhoff, K.; Mott, J.; Pfeiffer, D.; Renner, J.; Schindler, H.; Sheharyar, A.; Shiell, N.; et al. Garfield++. Available online: https://garfieldpp.web.cern.ch/garfieldpp/ (accessed on 10 June 2020).

29.   Tarrant, A. Development of Gas Electron Multipliers (GEMs) for Hybrid-Readout Gaseous Time Projection Chambers in Future Neutrino Experiments. Ph.D. Thesis, Royal Holloway University of Londonät Egham (UK), Egham, UK, 2020.

30.   DeLoach, R. *A Study of the Feasibility of Applying Capacitive Displacement-measuring Techniques to Open-mesh Grid Structures*; NASA Technical Note (TN); NASA: Washington, DC, USA, 1971.

31.   Bergström, K.; Sunner, S. The Relative Permittivity of Argon, Carbon Dioxide, and Hydrogen, Determined at 10 kHz Using a Transformer Bridge Method. *Phys. Scr.* **1976**, *13*, 51–52. [CrossRef]